Thermal Science and Engineering Progress 45 (2023) 102072

Contents lists available at ScienceDirect

Thermal Science and Engineering Progress

journal homepage: www.sciencedirect.com/journal/thermal-science-and-engineering-progress

Sulfur-induced transitions of thermal behavior and flow dynamics in laser powder bed fusion of 316L powders

Zhiyong Li [a,c,1], Xiuli He [a,c,*], Shaoxia Li [a,c], Xinfeng Kan [d], Yanjun Yin [e], Gang Yu [a,b,c,*]

[a] Institute of Mechanics, Chinese Academy of Sciences, Beijing 100190, China
[b] China Center of Materials Science and Optoelectronics Engineering, University of Chinese Academy of Sciences, Beijing 100049, China
[c] School of Engineering Science, University of Chinese Academy of Sciences, Beijing 100049, China
[d] Jiangsu University of Science and Technology, Zhenjiang 212100, Jiangsu, China
[e] Changzhou Institute of Technology, Changzhou 213032, Jiangsu, China

ARTICLE INFO

Keywords:
Melt pool dynamics
Thermal behavior
Fluid flow
Surface-active element
Laser powder bed fusion
3D printing and additive manufacturing

ABSTRACT

A three-dimensional (3D) powder-scale model is developed to analyze the melt pool dynamics in laser powder bed fusion (L-PBF) of 316L powders considering the transition of melt pool dynamics induced by sulfur element. In sulfur-free situation, thermal behavior and fluid flow are modeled involving 3D details. In sulfur-considered situation, sulfur-effect on melt pool dynamics is simulated with the surface tension described by the function of local temperature and the sulfur content. It is concluded that heat transfer is dominated by convection flow, and surface tension is the most important driving force. When the sulfur-effect is absent, surface tension increases from center to the periphery, inducing a centrally outward Marangoni convection. In the situation of 0.03% sulfur, surface tension first increases then decreases from center to the boundary, resulting in the novel flow pattern of combined outward-inward flow. Probing the underlying physical details induced by sulfur-effect, it makes melt pool dynamics more complex with more vortexes, and the sulfur-induced backward branch flow at the transverse view is benefit for the reduction of surface roughness. Furthermore, more vortexes, more branch flow, and more mixing positions of branch flow (MPBF) are observed in the sulfur-considered situation, which induces the increasing flow complexity, the drop of temperature gradient and driving force, as well as the decreasing flow intensity. Moreover, the variation of sulfur content leads to significant transitions of thermal behavior, driving force, and dynamic characteristics. Fundamental conclusions contribute significantly to the comprehensive understanding of the physical process in L-PBF of 316L powders.

1. Introduction

Laser powder bed fusion (L-PBF) is identified as one of the most promising metal additive manufacturing (AM) processes with the advantages of complex geometry, printing efficiency, and structuring performance [1–3], etc. Thus, L-PBF has drawn numerous attention from the communities such as aerospace, healthcare, shipbuilding, and energy industry, etc. Whereases, its widespread applications are faced with some major challenges arising from unexpected process-related defects, such as balling, pores, and hot cracking [4–6], etc. Among many underlying causes that restrict the wide acceptance of L-PBF, unexpected melt pool dynamics have been recognized as one of the significant reasons for process-induced structure defects [4–8]. Therefore, extensive efforts should be devoted to revealing the mechanisms of melt pool dynamics in L-PBF, probing potential approaches to mitigate unexpected processes, and achieving the process adjustment for quality improvement.

Direct optical observations of melt pool dynamics using imaging technologies like the high-speed high-energy X-ray imaging can provide reliable online results. Thus, various imaging devices and tools have been developed and promoted in the experimental observation of melt pool dynamics in L-PBF [9–12]. Melt pool evolution together with powder spattering was directly observed by Guo et al. [9] through the self-developed in-situ X-ray imaging device in Argonne National Laboratory (ANL), and the evolution of melt pool morphology, as well as keyhole formation versus time variable, was obtained with high-

* Corresponding authors at: Institute of Mechanics, Chinese Academy of Sciences, Beijing 100190, China.
E-mail addresses: xlhe@imech.ac.cn (X. He), gyu@imech.ac.cn (G. Yu).
[1] Currently working in Welding and Additive Manufacturing Centre, Cranfield University, Cranfield MK43 0AL, Bedfordshire, UK.

https://doi.org/10.1016/j.tsep.2023.102072
Received 9 March 2023; Received in revised form 4 July 2023; Accepted 16 August 2023
Available online 19 August 2023

resolution. An online observation facility equipped with fast camera was established by Gunenthiram et al. [10] to analyze the melt pool dynamics in L-PBF. The droplet formation and powder spattering were optically captured, and it was revealed that lower heat input contributes to the reduction of spattered powders. Additionally, optical pyrometer [13] and infrared thermography [14] had also been demonstrated as useful tools for in-situ observation of melt pool dynamics in L-PBF. Though insightful knowledge can be gained from in-situ imaging using optical and thermal technologies, experimental observations lack sufficient dynamics details due to the restrictions of imaging mechanism and device capability, as well as restricted by the weakness of being time-consuming and cost-consuming.

Contributed to the fast development of the modeling method, numerical simulation makes it possible to directly describe the thermal behavior and flow dynamics with sufficient physical details supporting the comprehensive understanding and the derivation of process-structure relations in L-PBF [15–20]. A systematic parametric study was numerically performed by Kan et al. [15] through a powder-scale dynamics model. It was found that the depth and width of the melt pool increase gradually with the increase of energy density. Besides, discontinuous and seriously spheroidized track can be observed when the input energy was below a key threshold. A transient 3D model was developed by Mukherjee et al [16] to investigate the heat transfer and fluid flow in L-PBF of commonly used materials including stainless steel, titanium, nickel, and aluminum-based alloys. It was concluded that small changes in hatch spacing did not significantly affect the cooling rate and the secondary dendrite arm spacing. Modeling prediction specifically aimed at high-density porosity in L-PBF of Ti6Al4V was carried out by Vastola et al [17], and a formula that described the emission of bubbles from the melt pool indentation and the probability of bubble trapping by the solidification front was obtained through the simulation work. The melt pool dynamics with complex flow pattern was numerically studied by Ge et al. [18] by a powder-scale transient model. The melt pool flow was driven by the semi-melted powders towards unmelted powders, leading to the non-uniformity of single track, while the fluid flow was driven by the near-fully melted powders towards the melt pool center, which increased the single-track uniformity. The obtained insights into melt pool dynamics from peer-reviewed publications have revealed the effects of processing parameters on the L-PBF process, such as laser power and scanning speed, the formation mechanisms of process-related defects including lack of fusion, porosity, and track non-uniformity, etc., and the dynamic evolution of track morphology related to the surface quality of as-built parts, which have made great contributions to the comprehensive understanding of the physic process and the derivation of process-structure relations in L-PBF. However, the physical details of fluid flow inside the melt pool have not been paid enough attention, especially the spatial and directional dynamic characteristics, which are the key reasons to explain why the specific unexpected structure such as micro-cracking, porosity, etc., occurs at the certain position, not other locations. Furthermore, the gained knowledge on spatial and directional melt pool dynamics can provide insights into the online monitoring and quality improvement of L-PBF.

Surface tension has been identified as one of the most important driving forces for melt pool dynamics in the above-cited works [15–20], in which the temperature coefficient of surface tension (TCST) is assumed as a negative constant, representing that the surface tension linearly decreases with the increasing of local temperature at gas/liquid surface. Whereas, in terms of printing materials for L-PBF, it can be classified into two categories according to the contained sulfur content, i.e., high-sulfur powders such as 316L and Inconel 718, and low-sulfur powders including Ti6Al4V and AlSi10Mg, which will lead to the transition of melt pool dynamics. Specifically, TCST is a variable in the general situation, and sulfur element contained in melted high-sulfur powders may induce the sign transition of temperature coefficient of surface tension (TCST) in certain temperature condition and surface-active element condition [21,22], as well as the transition of thermo-capillary force. The so-called surface-active element represents the six group elements including oxygen, sulfur, selenium, etc. For the L-PBF of 316L powders in the current study, only the surface-active element of sulfur is considered and analyzed because higher content of the sulfur element is inevitable for the metallurgy process of 316L stainless steel in comparison with other commonly used printing materials such as Ti6Al4V and AlSi10Mg. In detail, when the sulfur-effect is considered, the sign transition of TCST may occur in certain conditions, e.g., from positive to negative value or the inverse transition [21,22]. As a result, the flow pattern of the melt pool including both the direction and magnitude will greatly change because surface tension is a non-negligible driver for melt pool dynamics.

The sulfur-induced transitions of TCST and flow pattern have drawn much attention from various laser manufacturing technologies of Fe-based and Ni/Co-based alloys, such as laser polishing of stainless steel [23], laser welding of stainless steel [24], and laser direct energy deposition of Co-based powders [25], etc., which share the similar physics with L-PBF. From the view of the mathematical description of TCST incorporated in proposed numerical models, TCST is expressed by a function of local sulfur content and temperature at the gas/liquid surface of the melt pool in [23–25], in which TCST is a variable and its sign transition from negative to positive or from positive to negative occurs, while it is just simplified as a negative constant in [15–20] and no sign transition is included. A 2D axisymmetric FEM model was proposed by Shen et al [23] to probe the mechanism of shape formation in laser melting of 304 stainless steel, in which temperature-dependent surface tension and TCST were calculated considering the sulfur content of 0.0072 wt%. The simulated results showed that liquid metal flows towards the area with greater surface tension and the free surface deformation was dominated by shear stress and normal stress. Oxygen-induced transitions of surface tension and flow features in laser keyhole welding of 42CrMo were modeled by Hu et al. [24]. TCST was a negative constant and convection flow inside the melt pool was centrally outwards when the welding process was protected by pure argon, while the TCST varied versus local temperature and liquid metal flowed from the melt pool boundary to the central area in air containing 21% oxygen. Gan et al. [25] established a 3D transient model to analyze the sulfur dilution and sulfur-induced transition of flow pattern during laser direct energy deposition of Co-based powders to 38MnVS substrate. It was revealed that melt pool morphology varied with the dilution of sulfur element under different laser power and mass flow rate, and the flow pattern with combined inward-outward flow was observed. In a word, the constant assumption of TCST is reliable for the modeling of the L-PBF process with low-sulfur powders, while not reasonable when simulating the melt pool dynamics for high-sulfur powders such as 316L. However, based on a comprehensive literature review [1–25], it can be concluded that the sulfur-induced transition of TCST and resultant transition of flow pattern in L-PBF of high-sulfur powders still have not been revealed by high-fidelity powder-scale multi-physics modeling, which is of great importance for physics understanding, process monitoring, derivation of process-structure relation, microstructure refinement, and quality improvement, etc.

To fill these gaps, an improved powder-scale melt pool dynamics model is developed for L-PBF of 316L, coupled with a sub-model describing the functional surface tension. The sulfur-free situation in which TCST is assumed as a positive constant is first modeled. The evolution of track morphology and melt pool dimension, transient temperature distribution, dimensional analysis of driving force, and the underlying mechanism of surface tension driving flow are separately analyzed, followed by the discussion of 3D spatial and directional features of flow dynamics. Next, melt pool dynamics for 0.03% sulfur situation are analyzed, involving the thermal behavior, sulfur-induced transitions of driving force and flow pattern, as well as the corresponding flow features at the same sections. The transition of flow pattern and dynamic features at 3D view are studied in detail to reveal the sulfur-effect on melt pool dynamics. Finally, a parametric study by

varying the sulfur concentration is carried out and gives an attempt to physically reveal the impact of sulfur content on melt pool dynamics for 316L powders produced in different countries or areas.

2. Model implement

2.1. Brief introduction of the model procedure

316L stainless steel has been widely applied in healthcare, offshore engineering, petrochemical, and automobile, etc. due to its excellent performance such as high strength, antioxidation, and good corrosion resistance, as illustrated in Fig. 1. Consequently, 316L powders also have drawn much attention from metal AM community.

A 3D transient powder-scale model based on Computational Fluid Dynamics (CFD) is put forward to simulate the melt pool dynamics in L-PBF. The CFD model is constructed on the software FLOW-3D and the secondary development involving the development of 316L powder bed, moving laser heat source, surface tension sub-model considering sulfur effect, etc., are conducted by the authors. Heat transfer, phase change, fluid flow, powder fusion, track formation, as well as the sulfur-induced transition of melt pool dynamics, are all modeled in the current simulation. Fig. 2 schematically shows the numerical procedure and modeling validation for the current study. 316L powders with the diameter range from 20 μm to 50 μm are randomly generated with an average layer thickness of 50 μm based on the Hertz-Midlin (no slip) method, and filled into the powder bed with the dimension of 1000 μm × 400 μm × 150 μm. The porosity rate of the powder bed is set as 0.44. It should be noted that the generation of powder layer contained in the proposed model refers to the real L-PBF process. The powder size and the corresponding fraction are included in the sub-figure of Fig. 2. To exclude the impact of the cell size of mesh system on modeling results, the mesh-sensitivity test has been first carried out by varying the cell size. Iteration calculation is performed with the minimum time step of 10^{-12} s by SIMPLE solver based on the finite volume method (FVM). Additionally, the 3D dynamics model is established based on some major assumptions. Fluid flow is Newtonian, laminar and incompressible under the Boussinesq approximation. The laser heat source is assumed as Gaussian distribution and ray tracing is not considered. Fluid flow in the mushy zone in which the temperature is between solidus and liquidus is porous flow and can be described by the Carmen-Kozeny relation [26,27]. Heat loss and mass loss, induced by vapored materials, are not considered because the current printing is under conduction mode, which will be discussed in Section 3. The thermal properties of 316L powders are considered sulfur independent.

Modeling of melt pool dynamics for L-PBF of 316L powders in the current study is classified as the sulfur-free situation and sulfur-considered situation. To gain insights into the sulfur-effect on melt pool dynamics and more importantly, on the process-structure–property relations, a parametric study of sulfur content is performed, using the variables in Table 1. The study cases are arranged in such a way that they can cover most of the standards for 316L stainless steel or equivalent alloys worldwide, as well as providing references for other materials used in metal AM, such as Inconel 718. The 0.03% sulfur-modified melt pool dynamics are first simulated in sulfur-considered situation and compared with the sulfur-free situation because it is the highest content in the current study and hopefully presents illustrative details. What is more, the nominal composition for sulfur is 0.03% max subject to the US ASTM AISI and SAE, EU EN, and France AFNOR [28], which is widely used in the global industry community.

2.2. Thermophysical properties, numerical constants, and processing parameters

A 3D transient model on powder-scale is developed to analyze the melt pool dynamics in sulfur-free and 0.03% sulfur situations, respectively. Thermal-physical properties of 316L powders, numerical constants, and processing parameters used in the simulation are all listed in Table 2.

2.3. Governing equations

Heat transfer, phase change, fluid flow, powder fusion, track formation, as well as the sulfur-effect on melt pool dynamics are all simulated in the proposed numerical model.

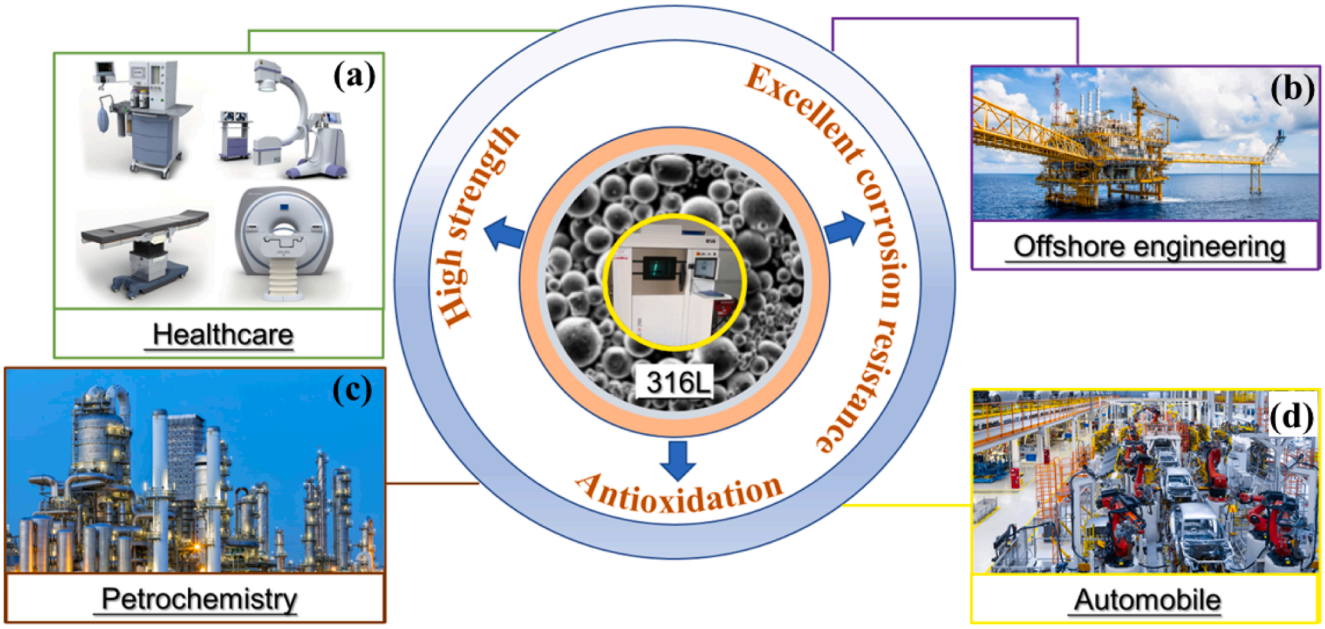

Fig. 1. Applications of 316L in the industry community. The website sources for sub-figures are (a) https://www.a2ztaxcorp.com/pondy-cm-questions-gst-on-medical-equipment-to-treat-virus/, (b) https://www.alara-lukagro.com/en/solution/oil-gas/, (c) https://www.arrayasolutions.com/why-manufacturers-iiot-strategies-fail-and-how-yours-can-succeed/manufacturing-plant/, and (d) https://www.thestatesman.com/business/auto-industry-woes-continue-coronavirus-likely-impact-component-supplies-china-1502854657.html.

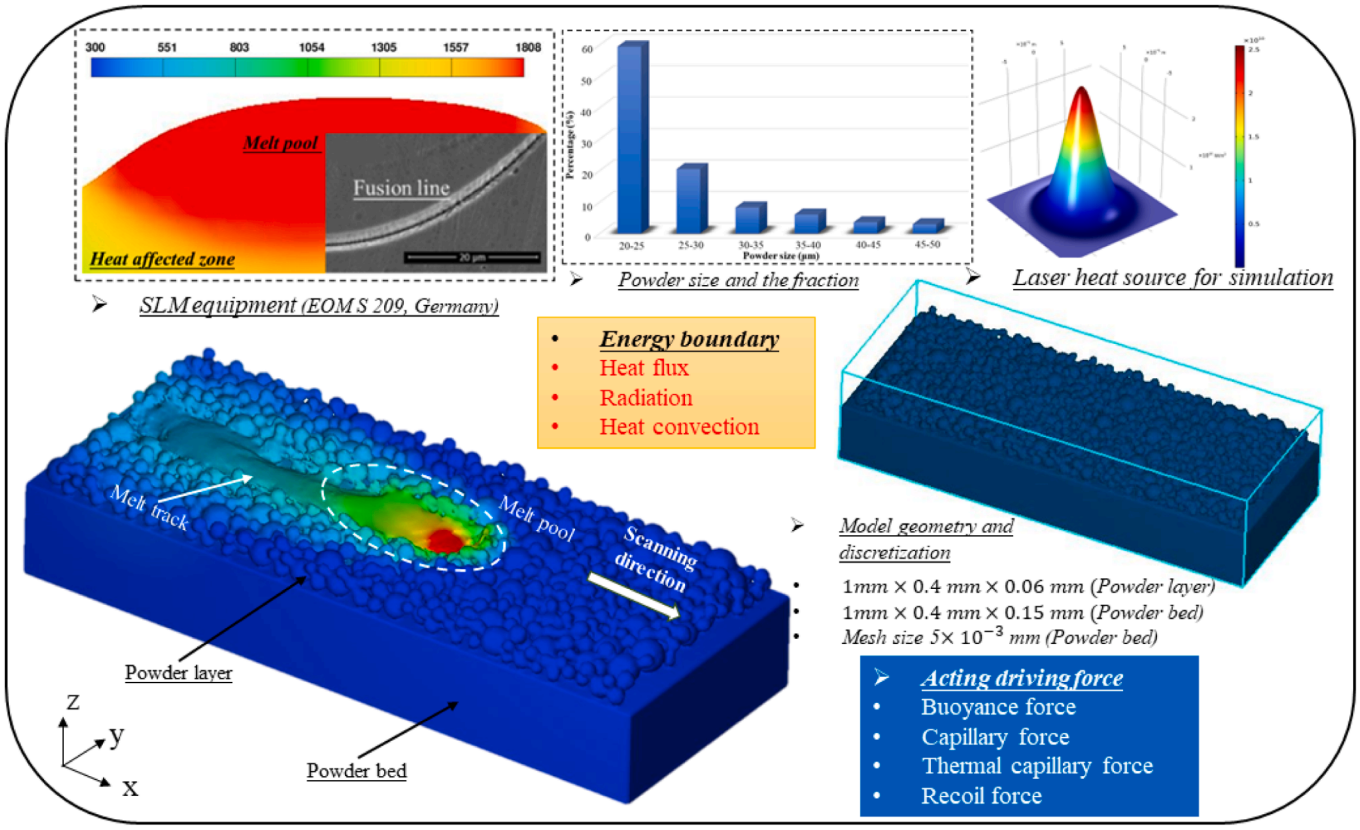

Fig. 2. Schematic diagram of the model implements, boundary condition, and experimental validation for the modeling of L-PBF of 316L powders. The experimentally observed melt pool morphology at cross-section is re-used from Ref. [15]. (For interpretation of the references to color in this figure legend, the reader is referred to the web version of this article.)

Table 1
Processing parameters and different cases for parametric study.

Processing parameters				Power (W)	Speed (mm/s)	Radius (μm)
				100	500	50
ID	Sul-1	Sul-2	Sul-3	Sul-4	Sul-5	Sul-6
Sulfur content (%)	0.0001	0.001	0.005	0.01	0.015	0.03

The fully coupled governing equations of mass, momentum, and energy conservation are respectively given as follows:

$$\nabla\cdot(\rho u) = 0 \tag{1}$$

$$\rho\frac{\partial u}{\partial t} + \rho(u\cdot\nabla)u = \nabla\cdot(\mu\nabla u) - \nabla p + \rho g - A_{mush}u(1-f_l)^2/\left(f_l^3 + M\right) \tag{2}$$

$$\rho C_p^{eq}\frac{\partial T}{\partial t} + \rho C_p^{eq}\mathbf{u}\cdot\nabla T = \nabla\cdot(K\nabla T) + \rho\frac{\partial(\Delta H)}{\partial t} - \rho\mathbf{u}\nabla(\Delta H) \tag{3}$$

In relations, ρ and $\mathbf{u}$ are the density of liquid metal and velocity vector, respectively. μ denotes the dynamic viscosity. Additionally, $\mathbf{p}$ is the fluid pressure and $\mathbf{g}$ is the gravitational acceleration vector. A_{mush} is a numerical constant determined by the mushy zone morphology, representing the dynamics restriction for porous flow, and set as $10^7 kg/m^3{\cdot}s$. f_l is the liquid phase fraction and expressed as $f_l = \frac{T-T_s}{T_l-T_s}$ according to the Carmen-Kozeny relation [26,27]. Particularly, it is zero below solidus (T_s) and one above liquidus (T_l). M is also a numerical constant used to avoid the division by zero when the liquid fraction f_l is zero, and it is set as 10^{-4}. T is the transient temperature of liquid materials. C_p^{eq} is the equivalent specific heat and expressed as:

$$C_p^{eq} = C_p + \frac{L_m}{\sqrt{\pi}\Delta T^2}\exp\left[-\frac{(T-T_m)^2}{\Delta T^2}\right] \tag{4}$$

where $\Delta T = (T_l - T_s)/2$ and $T_m = (T_l + T_s)/2$, denoting the solidification interval and the melting temperature, respectively.

Additionally, K represents the thermal conductivity and $\Delta H = L_m f_l$ is the specific enthalpy induced by phase change, in which L_m and f_l are the enthalpy of fusion and fraction of liquid phase, respectively.

2.4. Boundary conditions

High-reliability modeling is largely determined by the boundary conditions, which are described as follows.

2.4.1. Energy boundary

The boundary condition of energy at gas/liquid surface, i.e., the top surface of melt pool, can be described as:

$$-K\frac{\partial T}{\partial z} = \frac{2\eta Q}{\pi {r_b}^2}\exp\left(-\frac{2r^2}{r_b^2}\right) - h_c\left(T - T_{ref}\right) - \sigma_b\varepsilon\left(T^4 - T_{ref}^4\right) \tag{5}$$

In Eq. (5), the first term at right hand is the heat input from laser heat source. η is the absorptivity of laser and Q is the laser power. r_b and r denote the effective laser radius and distance to the center of laser spot, respectively. r is the function of laser scanning speed v and irradiation time t. Moreover, the second term and third term at right hand denote the heat convection and radiation, respectively, which contribute to the heat loss in L-PBF. h_c is the heat transfer coefficient of convection, σ_b is the Stefan-Boltzmann constant and ε is the emissivity.

For the energy condition at the bottom surface and other side

Table 2
Thermophysical properties of 316L powders, numerical constants, and processing parameters in modeling L-PBF [29–31].

Properties for 316L powders				
Property	Symbol	Unit	Value	Reference
Specific heat in solid	C_p	J/kg/K	755	[29]
Specific heat in liquid	C_p	J/kg/K	$462 + 0.134 \times T$	[29]
Density in liquid	ρ	kg/m^3	$7433 + 0.0393 \times -1.8 \times 10^{-4} \times T^2$	[29]
Density in solid	ρ	kg/m^3	$8084 + 0.4209 \times T - 3.9 \times 10^{-5} \times T^2$	[29]
Thermal conductivity in solid	K	W/m/K	$12.41 + 0.003279 \times T$	[29]
Thermal conductivity in liquid	K	W/m/K	$9.248 + 0.01571 \times T$	[29]
Solidus temperature	T_s	K	1788	[30]
Liquidus temperature	T_l	K	1808	[30]
Enthalpy of fusion	L_m	kJ/kg	247	[31]
Dynamic viscosity	μ	Pa s	6.0×10^{-3}	[31]
Temperature coefficient of surface tension	γ	N/m/K	-4.3×10^{-4}	[31]
Surface tension	σ	N/m	1.7	[31]
Numerical constants				
Constant	Symbol	Unit	Value	Reference
Reflectivity	R_λ	1	0.7	–
Ambient temperature	T_{ref}	K	300	–
Heat transfer coefficient of convection	h_c	W/m^2/K	100	–
Stefan-Boltzmann constant	σ_b	W/m^2/K	5.67×10^{-8}	–
Emissivity	∈	1	0.2	–
Processing parameter				
Parameter	Symbol	Unit	Value	Reference
Laser power	P	W	100	–
Laser radius	r	μm	50	–
Laser scanning speed	v	mm/s	500	–
Powder layer thickness	h	μm	50	–

surfaces, only the second and third term of Eq. (5) are considered, which represent the convection and radiation heat loss, respectively.

2.4.2. Momentum boundary

The gas/liquid surface in L-PBF is curvature and captured by Volume of Fluid (VOF) method in current simulation [32]. Momentum condition acting on gas/liquid surface of the melt pool can be described by:

$$\left[-p\mathbf{I} + \mu\left(\nabla\bar{\mathbf{u}} + (\nabla\bar{\mathbf{u}})^T\right) - \frac{2}{3}\bar{\mathbf{u}}(\nabla\cdot\bar{\mathbf{u}})\mathbf{I}\right]\cdot\vec{\mathbf{n}} = \sigma\kappa\vec{\mathbf{n}} + \gamma\nabla_s T \tag{6}$$

On right hand, the first term represents capillary force, and the second term denotes thermal capillary force. σ is the surface tension, κ is the gas/liquid surface curvature and γ is the temperature coefficient of surface tension (TCST).

2.5. Volume of fluid (VOF) method

Incorporated in the proposed melt pool dynamics model, VOF method is used to capture the powder fusion and track morphology, which can be expressed by [32]:

$$\frac{\partial F}{\partial t} + \nabla\cdot(F\mathbf{u}) = 0 \tag{7}$$

In relation, phase fraction F is calculated in each cell, while fluid velocity **u** is obtained from momentum equation Eq. (2). Thus, free surface of melt pool can be reconstructed in each iteration by the calculation of phase fraction.

2.6. Sub-model of surface tension

As discussed, surface tension and temperature coefficient of surface tension (TCST) are the function of local temperature and sulfur content for current modeling. The mathematical relation of surface tension/TCST, local temperature, and sulfur content is obtained by the work from Sahoo et al [21].

$$\sigma(T) = \sigma - \gamma(T - T_l) - R_u T\Gamma_s \ln(1 + K\alpha_s) \tag{8}$$

$$\frac{\partial\sigma}{\partial T} = -\gamma - R_u\Gamma_s\ln(1 + K\alpha_s) - \frac{K\alpha_s}{1 + K\alpha_s}\cdot\frac{\Gamma_s\Delta H^0}{T} \tag{9}$$

$$K = k_l\exp\left(-\Delta H^0/R_u T\right) \tag{10}$$

In relations, R_u is universal gas constant, Γ_s is the surface excess at saturation, k_l is the constant of segregation entropy, and ΔH_0 is the standard heat of adsorption. Referencing the published literatures [33,34], Γ_s is 1.3×10^{-5} Kmol/m^2, k_l is 3.18×10^{-3}, and ΔH^0 is -1.88×10^5 KJ/kmol in current modeling. α_s denotes the sulfur activity and is represented by the percentage of sulfur content, which is the constant of 0.03%. Consequently, both the surface tension and TCST are the function of local temperature and sulfur content. Different from the constant TCST with negative value when sulfur-effect is not considered, the TCST changes in every time step and the sign transition may occur in certain situation, e.g., the transition from positive to negative value or the inverse transition. In sulfur-free situation, the last term at right hand of Eq. (8) is not considered and the last two terms of Eq. (9) disappear, which results in the constant TCST with negative value.

This simplified TCST is widely used in the simulation studies of welding [35–37] and additive manufacturing [15–20,38–40]. It is reasonable in the printing of materials with ultralow content of sulfur, such as Ti6Al4V and AlSi10Mg. Whereas the general description of TCST as variable and the function of local temperature and sulfur-content should be paid enough attention when the powders with relatively high content of sulfur-active element are additively manufactured. e.g., the 316L powders with the nominal 0.03% max sulfur content, because the contained sulfur element will induce the sign transition of TSCT in certain temperature condition, resulting in the variations of flow pattern, transient thermal behavior, solidification process and microstructure, etc.

2.7. Mesh independency test

Mesh system for the current modeling is not selected randomly and the discretization with uniform 5×10^{-6} m element refers the setup from publications [32,38]. It should be noted that the mesh system should guarantee the reliable discretization in comparison with the real powder bed. The mesh system with larger size such as 1×10^{-5} m cannot accurately discretize the model geometry.

As listed in Table 3, the modeling with 3×10^{-6} m mesh system is conducted. The peak temperature and the maximum velocity change little between these two meshes, though the number of elements has largely increased from 895,442 to 4,004,777. Considering both the convergency and calculation efficiency, the simulation has been carried

Table 3
Comparison of the simulation results under different mesh systems in sulfur-free situation.

Maximum size of tetrahedral mesh (m)	Number of elements	Peak temperature(K)	Maximum velocity(m/s)
5×10^{-6} m	895,442	4460	3.35
3×10^{-6} m	4,004,777	4506	3.10

out on the mesh system with the maximum size of 5×10^{-6} m.

3. Results and discussion

3.1. Thermal behavior in the sulfur-free situation

Melt pool evolution and single-track morphology in sulfur-free situation are plotted in Fig. 3. Melt pool profile is denoted by the liquid region label that ranges from zero to one for the solid phase and liquid phase, respectively. As shown at the initial stage in Fig. 3(a), melt pool is formed after a short time of irradiation from the laser heat source. The volume power density of the laser beam in L-PBF can be expressed as $E = P/vdh$. E, P, v, d, and h represent the volume power density, laser power, scanning speed, hatching space, and powder layer thickness, respectively. Compared with the laser direct energy deposition (L-DED), the power density of L-PBF is much higher because of the ultra-small laser spot [4,25]. Ultra-high power density induces the quick formation of the melt pool, while ultra-fast scanning speed results in quick solidification. In the comparison with the stable melt pool in Fig. 3(c), the melt pool at the initial stage in Fig. 3(a) is shallow together with small length. However, the width of the melt pool changes little from Fig. 3(a)–(c). With processing, the melt pool length increases because of the ultra-fast scanning speed, and melt pool depth also grows due to more melted materials. Finally, the melt pool reaches the quasi-stable stage as plotted in Fig. 3(c), at which melt pool dimensions are almost unchanged.

Fig. 4 shows the temperature and velocity field for the stable melt pool in the sulfur-free situation. L-PBF can be classified into conduction mode and keyhole mode by evaporation-induced keyhole dynamics. For keyhole mode, the peak temperature inside the melt pool exceeds the boiling point and intense evaporation occurs due to the ultra-high input power density [9]. The gas/liquid surface will be significantly depressed due to the recoil pressure from vapored materials. The defects including porosity are prone to occurring in keyhole mode because of the unstable flow dynamics. For the conduction mode, material evaporation is not significant due to lower power density. The absorbed laser energy will be transported to inner powders and substrate by conduction. L-PBF process in the current work can be identified as conduction mode by the low power density. Moreover, temperature isolines in Fig. 4(a) are distributed with circular shape, which is recognized as the typical features of heat conduction [19]. Transverse distribution of temperature and velocity field when melt pool reaches quasi-stable stage is illustrated in Fig. 4(b). In sulfur-free situation, surface tension continuously decreases with temperature increment. As a result, the central area presents smaller surface tension, though the local temperature is higher. In contrast, surface tension is higher at the melt pool periphery with lower temperature. As shown in Fig. 4(b), a centrally outward Marangoni convection is driven in the sulfur-free situation, corresponding to the increasing direction of surface tension. Interestingly, the velocity magnitude, represented by the length of black arrows, also grows from the center to the periphery.

The 3D melt pool profile with temperature distribution is extracted in Fig. 4(c) to give more physical details, which shares the same scale bar with Fig. 4(a). The high-temperature region (red color) coincides with the area directly irradiated by laser beam. Additionally, the temperature at front part is much higher because the head area is being heated while the back area is under cooling. 3D velocity distribution is depicted in Fig. 4(d). Specifically, high-velocity regions randomly distribute at different positions of the melt pool.

Dimensional analysis is a powerful tool to probe the coupled impacts of processing parameters, such as laser power, powder layer thickness, scanning speed, etc., and physical properties of materials, such as thermal conductivity, dynamics viscosity, etc., on the process-structure–property (PSP) relations for metal AM, including heat transfer, phase change, fluid flow, solute dilution, solidified microstructure, grain growth, ultimate tensile strength, etc. [4]. Several key dimensionless numbers are thus obtained by combing different sets of variable groups, which can help reduce the total considerable variables and provide insights into the above-mentioned physics. Some key dimensionless numbers commonly used in the description of melt pool dynamics of L-PBF are summarized in Table 4, in which significance, mathematical expression, and calculated magnitude at different stages are all discussed.

First is the heat transfer Peclet number, representing the relative importance of convection to conduction in heat transfer. In relation, U and L are the characteristic velocity and characteristic length, which are denoted by the maximum velocity and half of the melt pool width, respectively. α is the thermal diffusivity, which can be expressed as $\alpha = K/\rho C_p$. Convective transfer overweighs heat conduction in L-PBF because Pe is over 10^1. However, the convective mechanism is more significant at the stable stage, which is consistent with the numerically [15,38] and experimentally [9] obtained knowledge that convection flow in L-PBF becomes stronger with the melt pool evolution from the initial stage to the stable stage.

Melt pool dynamics is driven by multiple forces including the surface force acting on the gas/liquid surface (surface tension) and the body force (buoyancy force). In the expression of Gr, β is the thermal coefficient of thermal expansion and ΔT is the difference between peak temperature and liquidus temperature. From the significance and calculated magnitude of Gr, it can be concluded that the buoyancy force is not strong enough to overcome the viscous restriction to drive the fluid flow. The modeled result of buoyancy force driven flow in laser welding of 304SS [23] is ultra-weak, which supports the above-obtained conclusions from dimensional analysis. From the obtained Ma, surface tension overweights viscous force. Combined with the ratio of Ma to Gr, buoyancy force is less important in the comparison with surface tension on the role of driving melt pool dynamics. Inspired by the related reports from welding community [20] and L-DED community [41], which share the similar physics with L-PBF, the mechanism of surface tension driven flow without the consideration of sulfur-effect in L-PBF can be summarized as follows. Under the irradiation of Gaussian laser beam, the temperature decreases from the center to the periphery of melt pool while the surface tension is smaller at the central area but larger near the melt pool boundary when TCST is negative constant (sulfur-free situation). As a result, a centrally outward Marangoni convection is prompted from the center towards melt pool boundary, corresponding to the increasing direction of surface tension. Furthermore, the velocity magnitude increases along the same direction.

3.2. Spatial and directional flow dynamics in sulfur-free situation

As discussed, printing quality of as-built parts is largely determined by the melt pool dynamics and significant quality factors including balling, porosity and cracking are strongly correlated with heat transfer and fluid flow inside melt pool [4,6]. Thus, the spatial and direction characteristics of melt pool dynamics at 3D view are simulated first without the consideration of sulfur-induced transition of TCST.

Fig. 5 shows the temperature and velocity field at three transverse sections located at the front, middle, and tail region of the melt pool, respectively. The positions of three transverse sections in Cartesian coordinates are labeled in Fig. 5(a). Particularly, the flow directions at different sections are highlighted by white solid arrows. At the front section 1, no vortex is formed but a branch flow towards the positive y-axis direction is observed. Besides, fluid flow is strong enough and reaching 2.47 m/s, which is beneficial for the transportation of absorbed energy from upper melted powders to bottom powders and substrate. At the middle section 2, one separate vortex is observed at right melt pool, accompanied by a rightward branch flow originating from left part. The branch flow at tail section 3 is consistent with that at sections 1 and 2, which is still towards the right melt pool.

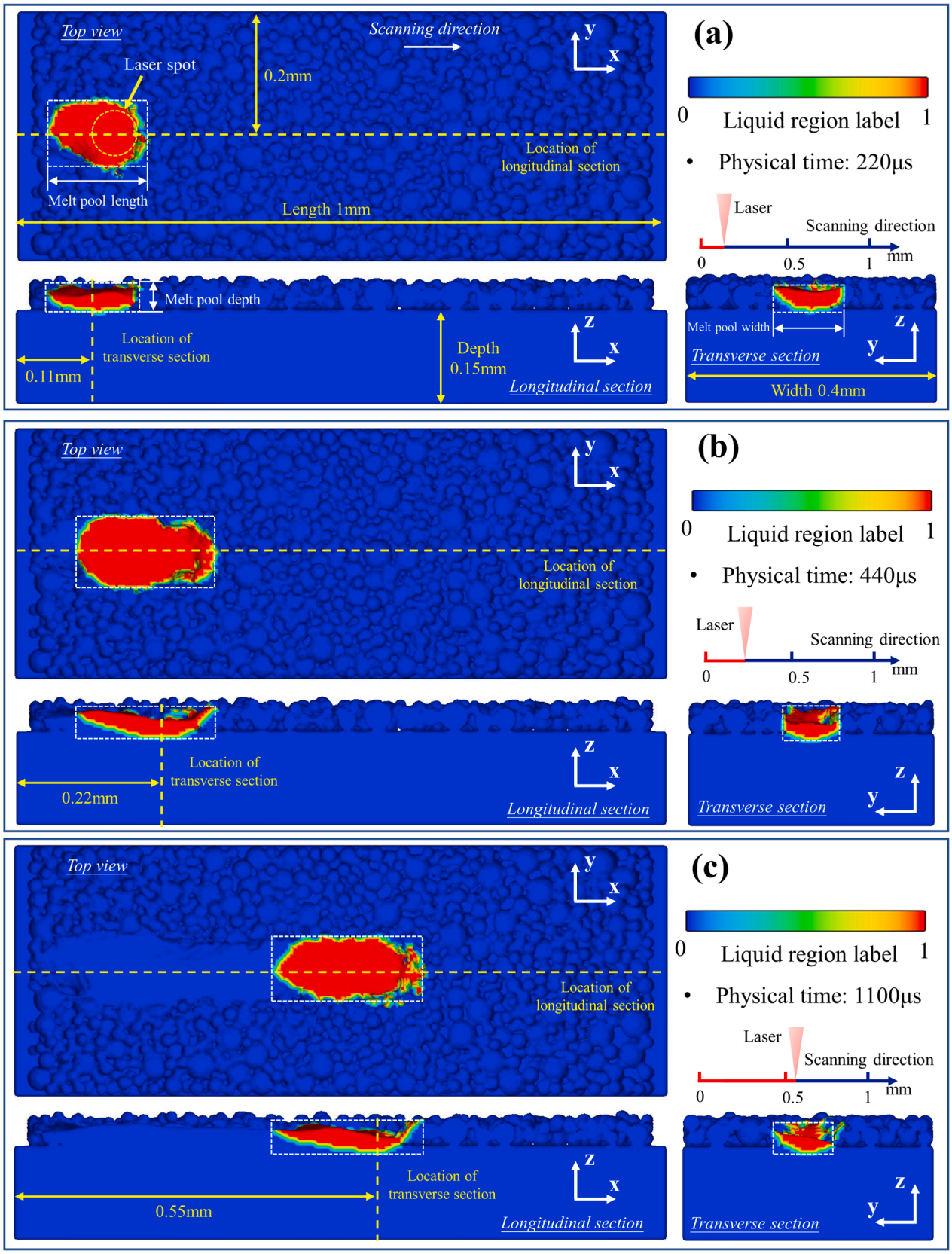

Fig. 3. Melt pool evolution and track morphology at the top view, longitudinal section, and transverse section in L-PBF of 316L powders without the consideration of sulfur-effect. The melt pool dimension is labeled by white dotted rectangle, and the position of the laser heat source is highlighted by yellow dotted circle. Positions of the longitudinal section and transverse section are illustrated by the yellow dotted line. Color contour represents the fraction of the liquid phase. Inset above transverse section describes the location of the laser heat source in the proposed model corresponding to the real physical time. (a) 220 μs, (b) 440 μs, (c) 1100 μs. (For interpretation of the references to color in this figure legend, the reader is referred to the web version of this article.)

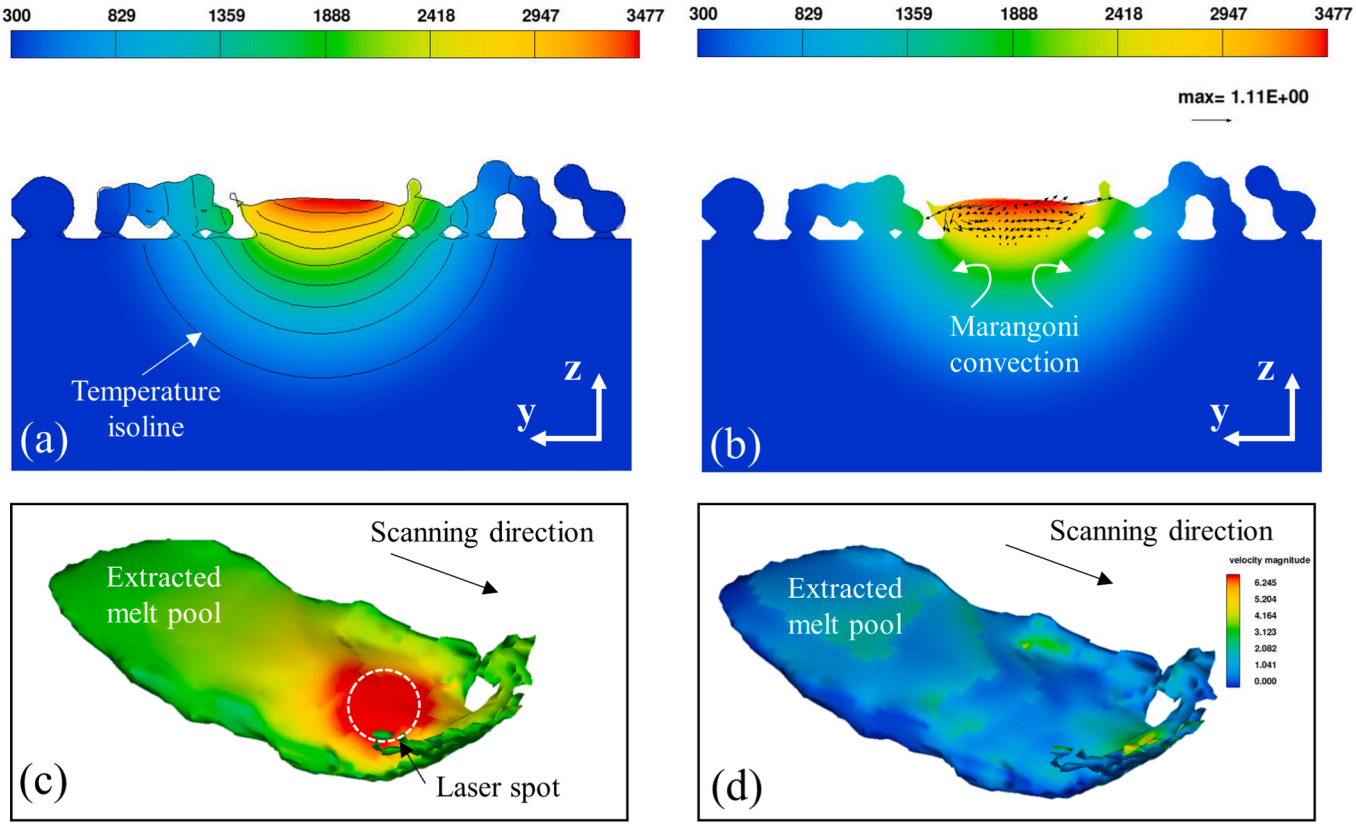

Fig. 4. Temperature distribution and velocity field at the stable stage in L-PBF of 316L powders without the consideration of sulfur-effect. (a) Temperature distribution in Kelvin with isolines. The 2D temperature field is denoted by color contour. (b) Temperature distribution with velocity field. The 2D temperature field is denoted by color contour, while the direction and magnitude of the velocity field (m/s) are represented by the direction and length of black arrows, respectively. (c) 3D temperature distribution. (d) 3D velocity field with magnitude expressed by the color bar. (For interpretation of the references to color in this figure legend, the reader is referred to the web version of this article.)

Table 4
Dimensionless numbers used to analyze the heat transfer and fluid flow in L-PBF of 316L powders.

Dimensionless numbers	Significance	Expression	Initial stage	Stable stage
Peclet number (Pe)	The ratio of convection to conduction	UL/α	10^1	10^2
Grashof number (Gr)	The ratio of buoyancy force to viscous force	$g\beta L^3\Delta T\rho^2/\mu^2$	10^{-1}	10^{-1}
Marangoni number (Ma)	The ratio of surface tension to viscous force	$\rho L\Delta T\lvert\partial\gamma/\partial T\rvert/\mu^2$	10^3	10^4
$Re_{Ma/Gr}$	The ratio of surface tension to buoyancy force	Ma/Gr	10^4	10^4
Reynolds number (Re)	The ratio of inertial force to viscous force	$\rho UL/\mu$	10^1	10^3

Denoted by the arrow length, the velocity magnitude at the transverse view obviously decreases from sections 1–3, indicating that fluid flow gradually becomes weaker from the front region to the tail part. The difference in spatial temperature gradient is one of the underlying contributors to the variation of velocity magnitude. As shown in Fig. 5 (a), the temperature near the melt pool tail is relatively high because this area has just undergone the melting and solidification process, while the powders near the front melt pool, which are not irradiated by laser, are still under ambient temperature (300 K). As a result, the spatial temperature gradient, which is the derivative of temperature in the spatial direction, is much larger in the front area compared to the tail region. Based on the knowledge derived from published literature regarding the driving forces for melt pool dynamics [43,44], temperature gradient determines the magnitude of thermal capillary force (Marangoni stress) when TCST is a constant. Furthermore, the thermal capillary force is positively correlated with the temperature gradient and governs the fluid flow [43,44]. As illustrated, the front region with higher temperature gradient induces larger driving force and stronger fluid flow.

Next, flow dynamics at longitudinal sections are analyzed together with the positions labeled in Fig. 6(a). At the longitudinal section 1, a significant vortex is observed at the tail melt pool and highlighted by white solid arrows. Velocity magnitude decreases from head region to tail part, which is consistent with the trend illustrated in Fig. 4. Moreover, a backward branch flow is observed, which transports melted materials backward and contributes to roughening of the melt track at the tail region. It should be noted that the roughness increment of melt track induced by this front-to-back branch flow is also observed in Electron-beam additive manufacturing (EBAM) [45]. Interestingly, the vortex at back region and the front-to-back branch flow are observed at all three longitudinal sections, though the velocity distribution significantly changes at different sections. Nevertheless, it can be inferred from the simulated results shown in Figs. 5 and 6 that the laser-induced melt pool in L-PBF is asymmetric due to the randomly distributed powders with a diameter range. The symmetric assumption with a direction vertical to printing toolpath, which significantly reduces the computational resources, can be employed in L-DED modeling [25], but it is not suitable for L-PBF simulation.

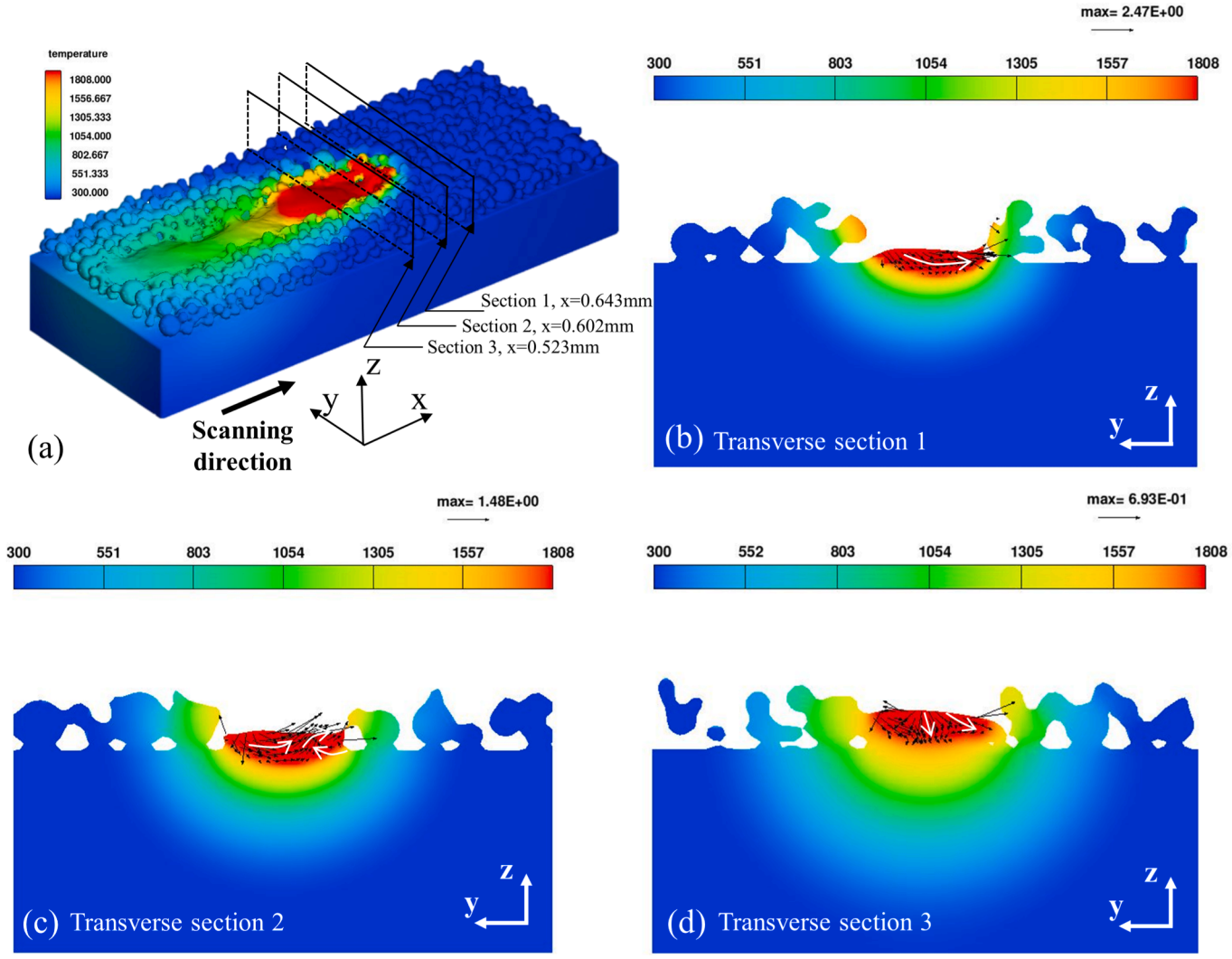

Fig. 5. Temperature distribution and velocity field at transverse view in sulfur-free situation when the melt pool is stable. The temperature field in Kelvin is represented by color contour. The flow direction and velocity magnitude (m/s) are depicted by the direction and length of black arrows, respectively. Positions of different transverse sections are labeled in (a) by the black rectangle. (a) 3D temperature distribution and velocity field. (b) Temperature distribution and velocity field at transverse section 1. (c) Temperature distribution and velocity field at transverse section 2. (d) Temperature distribution and velocity field at transverse section 3. (For interpretation of the references to color in this figure legend, the reader is referred to the web version of this article.)

To obtain a comprehensive understanding of melt pool dynamics, the fluid flow should be studied at three-dimensional views. In this part, flow dynamics at three z-axis sections, as shown in Fig. 7(a), are illustrated in Fig. 7(b)–(d), respectively. At z-axis section 1, melt pool is not complete with a large blank space in the middle area due to the lack of materials. The fluctuation of the top surface of the powder layer, resulting in voids between powders, explains the blank area of melt pool at this z-axis section. Furthermore, the backward branch flow, as illustrated in Fig. 6, which transports melted materials from the front area to the back region, also contributes to the formation of the blank area shown in Fig. 7(b). At z-axis section 2, blank space is significantly reduced because melt pool has been fully developed, accompanied by the homogeneous mixing of melted powders and melted substrate. At z-axis section 3, no blank area is observed because the substrate is continuous without voids between powders.

No vortex is found at the three z-axis sections, but the branch flows towards different directions are observed and highlighted by white solid arrows. At section 1, the branch flow transfers liquid materials forward, and is benefit for the decreasing of surface roughness of melt track, as the tail region undergoes forthcoming solidification. The branch flow at section 2 can be classified into two categories: positive and negative direction flow along the y-axis. On one hand, it has been reported that this mixing resulted from the two opposite branch flows contributes to the reduction of process-induced structure defects, such as porosity [46]. Similar branch flows have also been observed at section 3, despite the significant reduction in the melted area. It is important to note that the fully developed melt pool at section 3, located on the substrate, is of great importance, indicating the successful metallurgical joining between the powder layer and the powder bed, or the adjacent two layers in multi-layer printing.

3.3. Sulfur-effect on melt pool dynamics in 0.03% sulfur situation

3.3.1. Sulfur-induced transition of temperature coefficient of surface tension (TCST)

As discussed, temperature coefficient of surface tension (TCST) is a variable in general situation [21], and varies with local temperature and the content of surface-active element, i.e., the sixth group element in periodic table including oxygen, sulfur, etc. Particularly, sulfur-effect on melt pool dynamics with the sulfur content of 0.03% is modeled in this part. The necessity of first simulating 0.03% sulfur case has been discussed at the beginning of Part 2 Model implement.

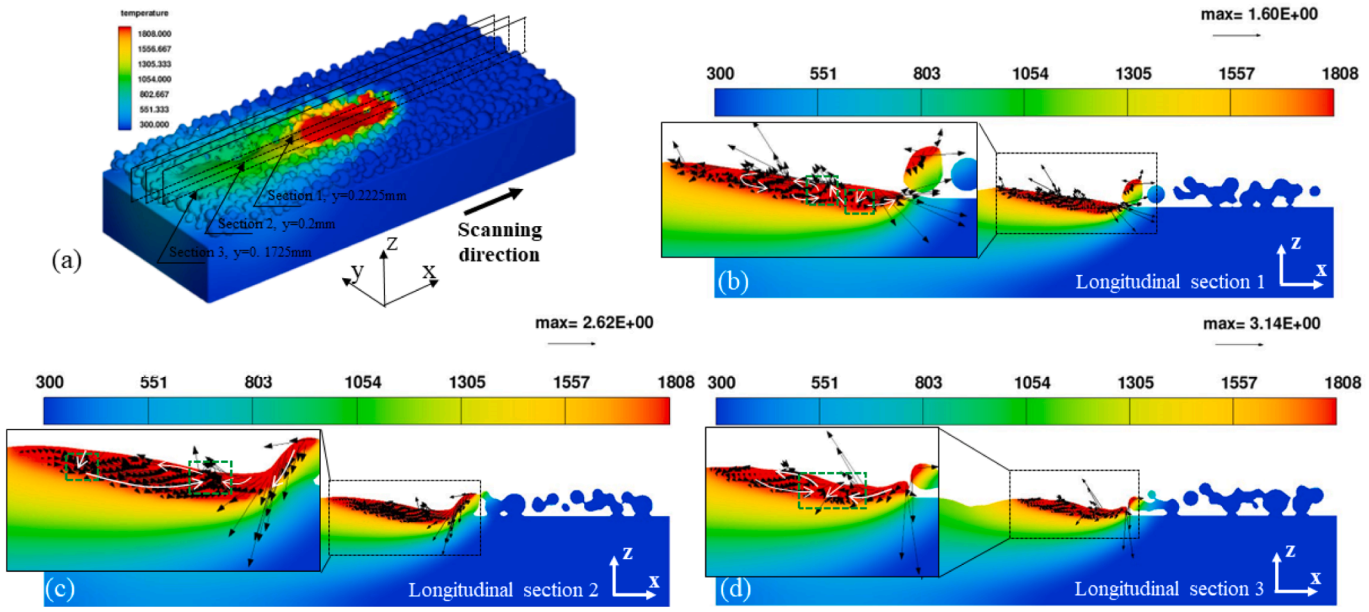

Fig. 6. Temperature distribution and velocity field at longitudinal section in sulfur-free situation when melt pool is stable. Temperature field in Kelvin is represented by color contour. Flow direction and velocity magnitude (m/s) are depicted by the direction and length of black arrows, respectively. Positions of different longitudinal sections are labelled in (a) by black rectangle. (a) 3D temperature distribution and velocity field. (b) Temperature distribution and velocity field at longitudinal section 1. (c) Temperature distribution and velocity field at longitudinal section 2. (d) Temperature distribution and velocity field at longitudinal section 3. (For interpretation of the references to color in this figure legend, the reader is referred to the web version of this article.)

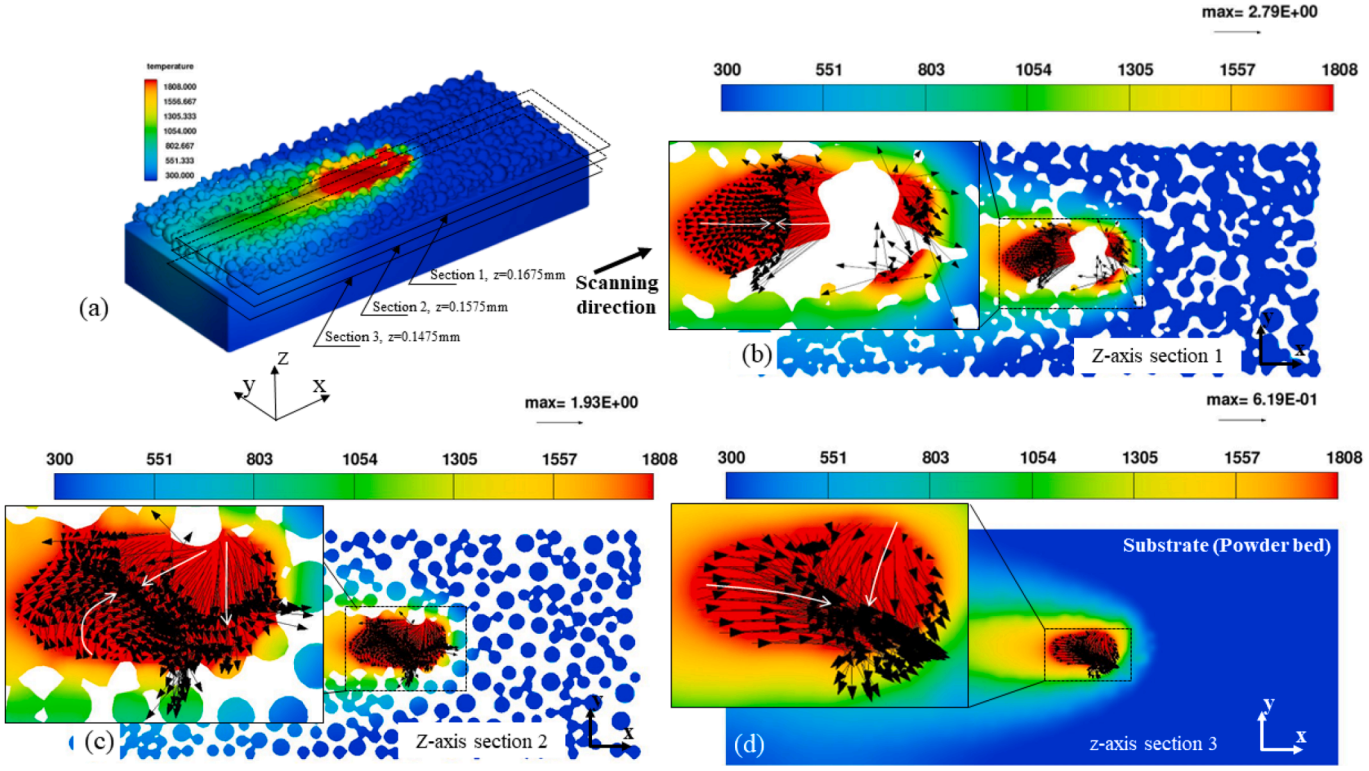

Fig. 7. Temperature distribution and velocity field at the z-axis section in sulfur-free situation when melt pool is stable. Temperature field in Kelvin is represented by color contour. Flow direction and velocity magnitude (m/s) are depicted by the direction and length of black arrows, respectively. Positions of different z-axis sections are labelled in (a) by black rectangle. (a) 3D temperature distribution and velocity field. (b) Temperature distribution and velocity field at z-axis section 1. (c) Temperature distribution and velocity field at z-axis section 2. (d) Temperature distribution and velocity field at z-axis section 3. (For interpretation of the references to color in this figure legend, the reader is referred to the web version of this article.)

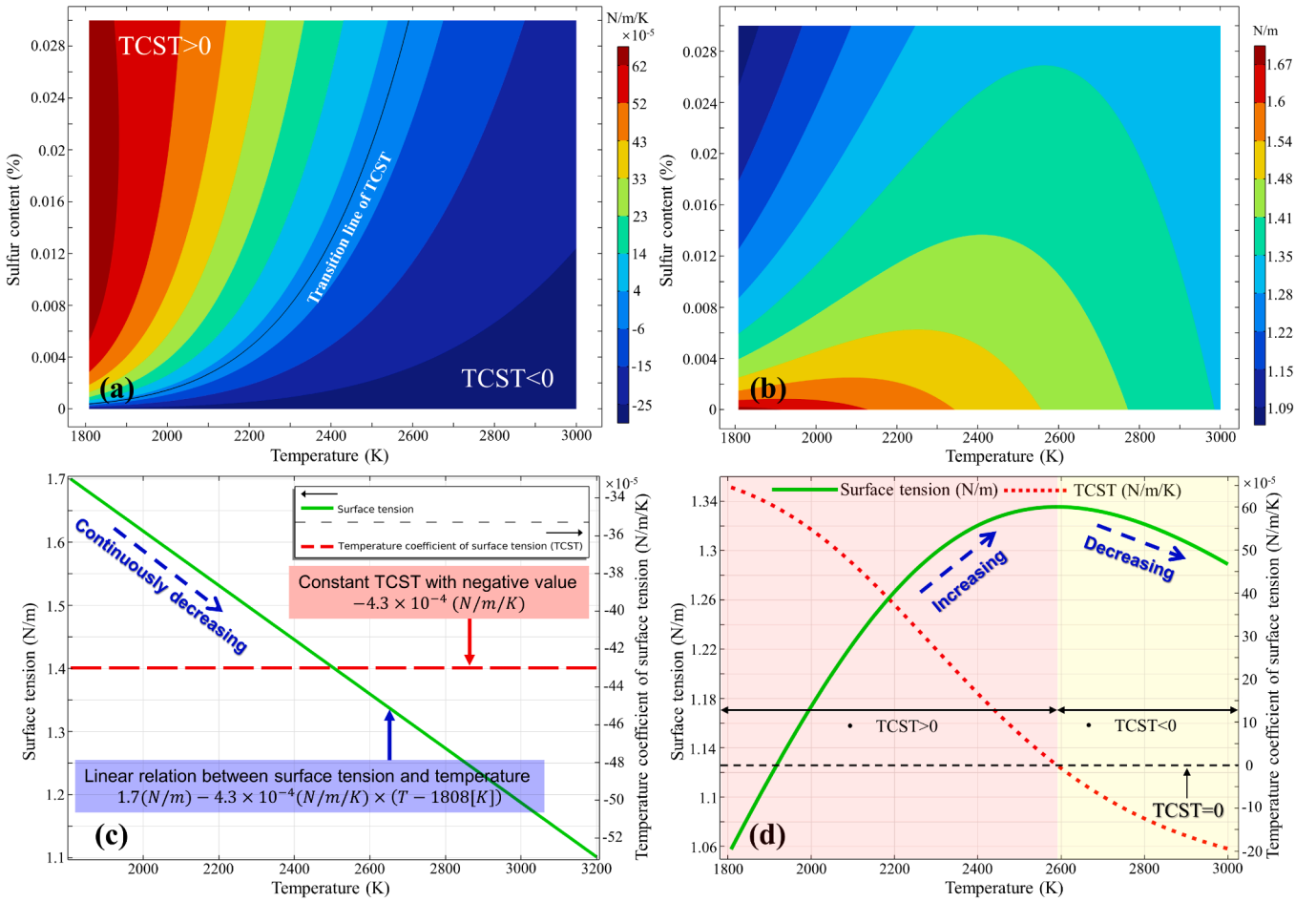

Fig. 8. Plot of surface tension and temperature coefficient of surface tension (TCST) of 316L powders as the function of local temperature in Kelvin and sulfur content in percentage. (a) TCST versus local temperature and sulfur content. Black line represents the transition of TCST from positive to negative value, and the TCST at transition line is zero. TCST denoted by color contour is positive upper transition line and negative at below area. (b) Surface tension versus local temperature and sulfur content. (c) Plot of surface tension and TCST versus local temperature in Kelvin in sulfur-free situation. (d) Plot of surface tension and TCST versus local temperature in Kelvin when sulfur content is 0.03%. (For interpretation of the references to color in this figure legend, the reader is referred to the web version of this article.)

The TCST of 316L powders versus local temperature and sulfur content is presented in Fig. 8(a), in which the transition of TCST from positive to negative value together with the transition line can be observed. In the situation of 0.03% sulfur content, TCST is positive at lower temperature and negative at higher temperature. Therefore, unlike the sulfur-free situation shown in Fig. 8(c) where the TCST of 316L powders is a negative constant and surface tension drops linearly with the increment of temperature, the surface tension of 316L powders first increases and then decreases in the sulfur-considered situation as the temperature continues to rise, as shown in Fig. 8(b) and (d).

The functional relations of TCST and surface tension in 0.03% sulfur situation are respectively plotted in Fig. 8(d). The TCST value of 316L drops from 6.07×10^{-4} N/m/K to -2.19×10^{-4} N/m/K, along with a sign transition from positive to negative, as the temperature changes from 1808 K to 3000 K. Consequently, the surface tension of 316L first increases to 1.34 N/m and then decreases to 1.05 N/m within the same range of temperature. Therefore, it is expected that sulfur-induced transition of TCST will result in the changes of flow pattern as it is largely driven by surface tension.

Fig. 9 showing the flow patterns under different TCST signs contributes to understanding the sulfur-induced transitions of flow patterns for six study cases in Table 1. In all the three situations, the temperature at the free surface is larger at the center and smaller at the edge, i.e., $T_{center} > T_{edge}$, as a result of the irradiation of Gaussian laser beam. When TCST is constantly negative, it represents that temperature increasing induces the drop of surface tension. Specifically, surface tension increases from the center to periphery with temperature increment, i.e., $\gamma_{center} < \gamma_{edge}$. Thus, fluid flow is towards melt pool boundary because it is always driven to the position with larger surface tension. For the situation of TCST (+), as shown in Fig. 9(b), surface tension becomes greater with temperature increasing. In specific, surface tension drops from center to melt pool edge with the increase of local temperature. i.e., $\gamma_{center} > \gamma_{edge}$. Accordingly, a flow toward center is driven by the inverse tendency of surface tension. As for the coexistence situation consisting of TCST (-) and TCST (+), it contains the physical processes of above-mentioned two situations. Surface tension first drops then increases from central area to melt pool boundary, and there is an inflection point under the transition temperature T_t at which the sign transition of TCST occurs. This transition leads to the fluctuation distribution of surface tension, i.e., $\gamma_{edge} < \gamma_t > \gamma_{center} < \gamma_t > \gamma_{edge}$. Based on the fact that surface tension driven flow is always originated from the area with lower surface tension and towards that with higher surface tension, an outward flow is observed in the melt pool center while an inward flow is driven near its edge. The sulfur-free assumption with the TCST of negative constant corresponds to the TCST (−) situation. As mentioned, sulfur-effect can induce the sign transition of TCST and the inverse tendency of surface tension. Consequently, the flow patterns illustrated in TCST (+) situation and coexistence situation are expected to be observed

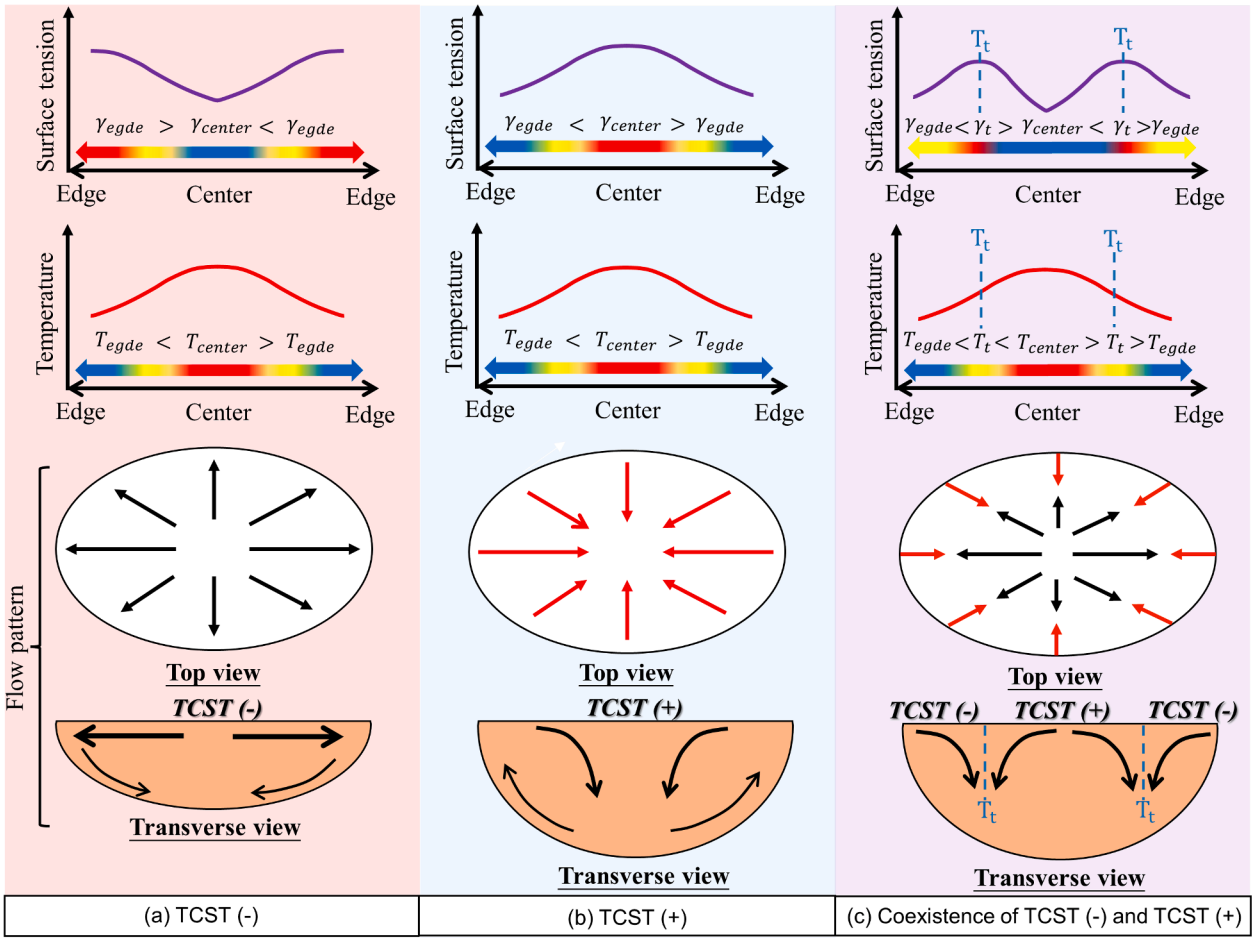

Fig. 9. Plot of the distribution of temperature and surface tension at the free surface of melt pool, as well as the flow pattern, under the sign variation of TCST. (a) TCST (−). (b) TCST (+). (c) Coexistence of TCST (−) and TCST (+). (For interpretation of the references to color in this figure legend, the reader is referred to the web version of this article.)

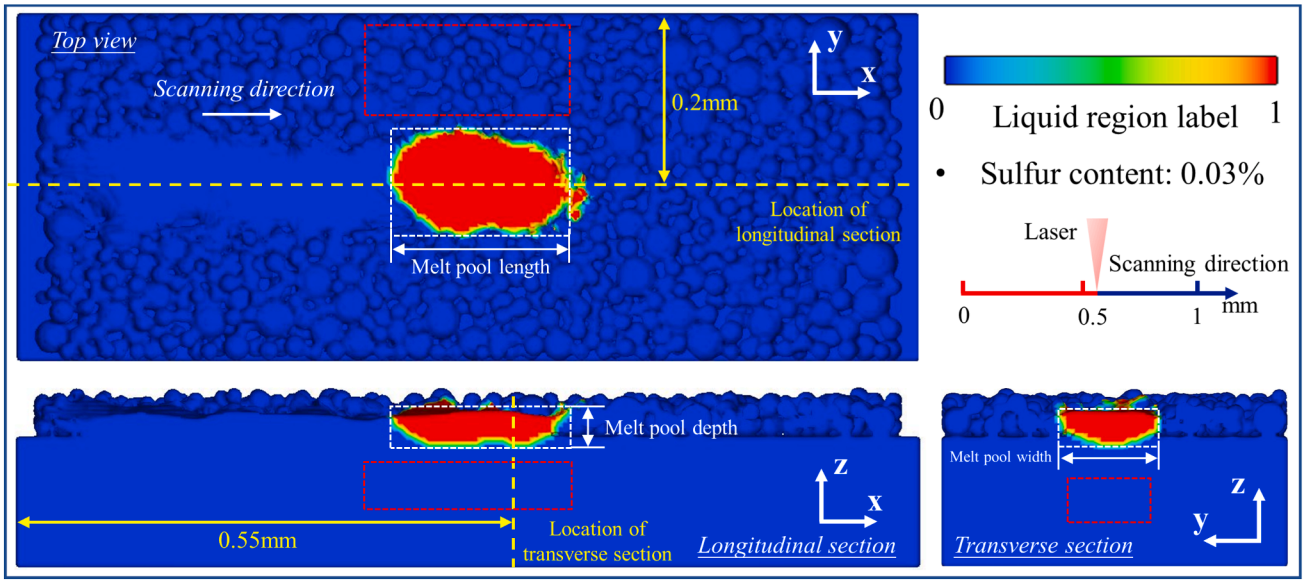

Fig. 10. Melt pool geometry and melted track morphology at stable stage in L-PBF of 316L powders with the consideration of 0.03% sulfur. Melt pool geometry in 0.03% sulfur situation is labelled by the white dotted rectangle, corresponding to the same physical time of 1100 μs. Positions of longitudinal section and transverse section are illustrated by the yellow dotted line. Color contour represents the fraction of liquid phase. Inset above transverse section describes the location of laser heat source in proposed model corresponding to the physical time. (For interpretation of the references to color in this figure legend, the reader is referred to the web version of this article.)

when sulfur-effect is considered.

3.3.2. *Sulfur-induced transition of thermal behavior*

Melt pool geometry and melted track morphology at the stable stage in 0.03% sulfur situation are plotted in Fig. 10. The modeling procedures for 0.03% sulfur including geometry, powder distribution, processing parameters, etc., are kept the same with sulfur-free situation. The red dotted rectangle in Fig. 10 denotes the melt pool geometry in sulfur-free situation at the same physical time. As illustrated, the melt pool length has significantly dropped in 0.03% sulfur situation. In contrary, the melt pool width presented in the transverse section has significantly increased. It can be predicted that the difference of thermal behavior when sulfur-effect is included is mainly attributed to the sulfur-induced transition of driving force, and the resultant transition of flow dynamics, which is the dominant mechanism for heat transfer.

Temperature distribution and velocity field at the stable stage in the 0.03% sulfur situation are plotted in Fig. 11(a) and (b), respectively. The zoom-in figures showing the temperature distribution and velocity field in 0.03% sulfur situation are plotted in Fig. 11(d) for a better understanding. As shown in Fig. 11(a), the tendency of temperature distribution denoted by isolines is similar to that in the sulfur-free situation shown in Fig. 4(a) and (c) (zoom-in). In specific, temperature isolines in Fig. 11(a) regularly distribute with circular shape, which indicates that melt pool dynamics in the 0.03% sulfur situation is still under the conduction-mode in spite of the sulfur-induced dynamics transition. Fig. 11(b) shows the velocity field at the transverse section when melt pool is stable. Compared with the results of the sulfur-free situation shown in Figs. 4 and 11(c) (zoom-in), the velocity magnitude has increased a lot, and the flow pattern has also changed significantly.

Surface tension distribution, the flow pattern, as well as the zoom-in temperature and velocity field, have been depicted in Fig. 11(c) for the sulfur-free situation and Fig. 11(d) for the 0.03% sulfur situation. The function curves in Fig. 11(c) and (d) are only used to qualitatively describe the trend of surface tension versus temperature. For the sulfur-free situation shown in Fig. 11(c), TCST is a negative constant [15–20,38–40,42], and a centrally outward flow is driven along the increasing direction of surface tension. In contrast, the function of surface tension in the 0.03% sulfur situation is nonlinear, along with the possible occurrences of negative and positive TCST at the same time. Specifically, surface tension drops with temperature increment for negative TCST while increases with temperature for positive TCST, corresponding to the coexistence situation illustrated in Fig. 9. In 0.03%

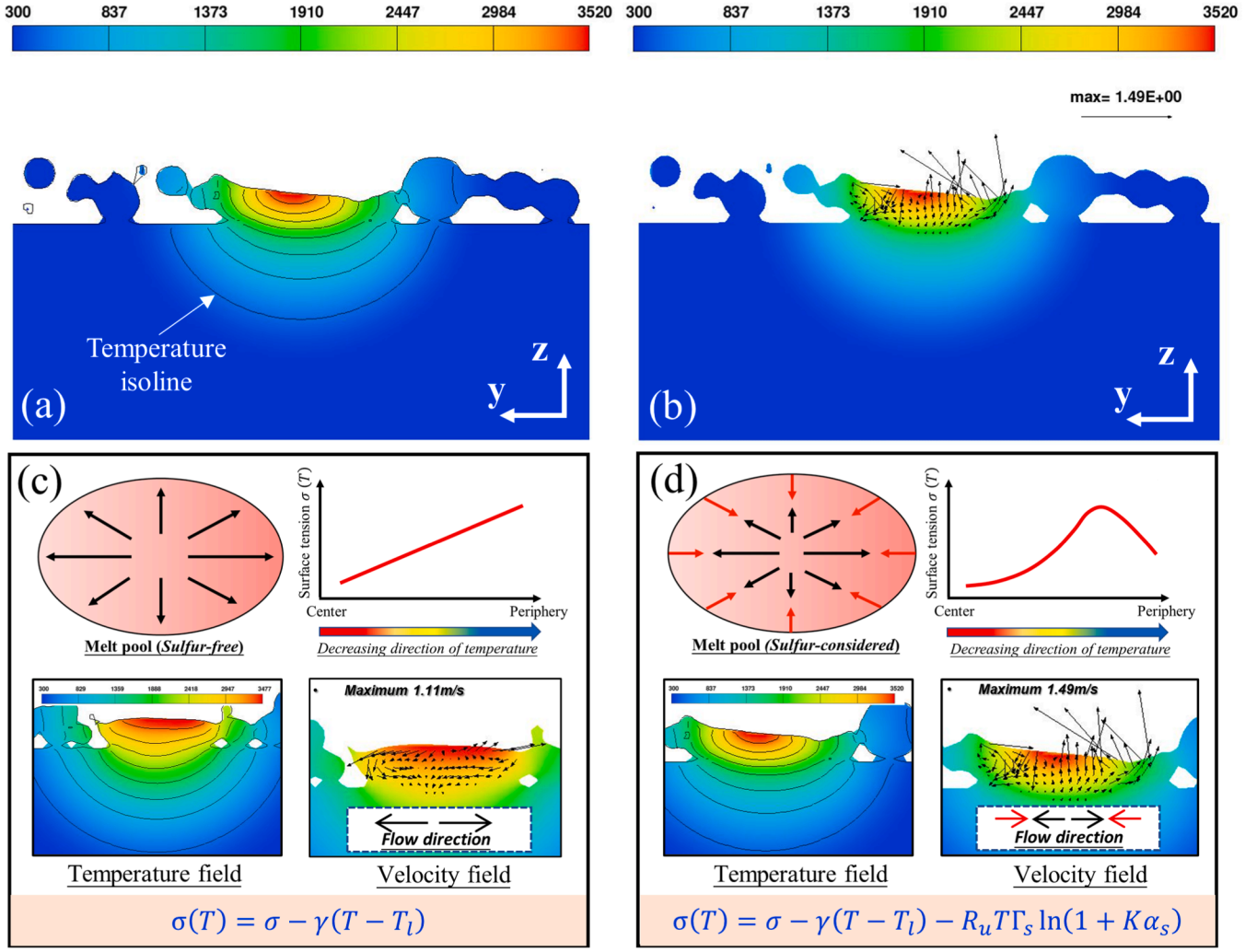

Fig. 11. Temperature distribution and velocity field at stable stage in 0.03% sulfur situation during L-PBF of 316L powders as well as the comparison with sulfur-free situation. 2D temperature field in Kelvin is denoted by color contour. Flow direction and velocity magnitude (m/s) at transverse section are represented by the direction and length of black arrows, respectively. (a) Temperature distribution with isolines in 0.03% sulfur. (b) Temperature distribution with velocity field in 0.03% sulfur. (c) Flow pattern, driving force, and zoom-in of the temperature distribution and velocity field in sulfur-free situation. (d) Flow pattern, driving force, and zoom-in of the temperature distribution and velocity field in 0.03% sulfur situation. (For interpretation of the references to color in this figure legend, the reader is referred to the web version of this article.)

sulfur situation, TCST is negative in central region of the melt pool but positive near its boundary, thus the sign transition of TCST is observed. As a result, surface tension first increases then drops with temperature increment from the melt pool center to its periphery, which induces the combined flow pattern in Fig. 11(d), as well as Fig. 9(c). For the stable melt pool with 0.03% sulfur, as shown in Fig. 11(b) and (d), a combined flow including the inward flow originating from the periphery and the outward flow originating from the center is observed. The zoom-in melt pool in the inset of Fig. 11(d) schematically illustrates the observed flow direction in 0.03% sulfur situation, which is consistent with the above-performed theoretical analysis of flow pattern form the view of driving force (surface tension) for flow dynamics.

3.3.3. *Sulfur-induced transition of spatial and directional flow dynamics*

Melt pool dynamics in the 0.03% sulfur situation is analyzed at 3D view to reveal the sulfur-induced transition of flow dynamics. Three transverse sections at the front, middle, and back part of the melt pool are plotted in Fig. 12 to show the temperature distribution and velocity field at the transverse view. The spatial positions of section 1, 2, and 3, as highlighted in Fig. 12(a), together with the processing parameters in the 0.03% sulfur situation are same as those in the sulfur-free situation. Flow directions at different sections are highlighted by white solid arrows. Following discussions come from the detailed comparison of melt pool dynamics between 0.03% sulfur situation and sulfur-free situation.

At transverse section 1, a new inward vortex is observed, and the branch flow towards the negative y-axis shown in Fig. 5(b) has changed to the opposite direction in Fig. 12(b). At transverse section 2, two separate downward vortexes shown in Fig. 12(c) are induced in 0.03% sulfur situation. In contrary, as shown in Fig. 5(c), only one upward vortex occurs at the transverse section 2 in sulfur-free situation. At transvers section 3, two separate downward vortexes with smaller velocity magnitude are observed in the flow pattern for 0.03% sulfur situation in Fig. 12(d), while no vortex is formed at the same section in the sulfur-free situation in Fig. 5(d). Therefore, it can be summarized that the melt pool dynamics in the 0.03% sulfur situation is more complex with more vortexes induced at different transverse sections. Moreover, the peak velocity at transverse view first increases then drops from section 1 to sections 2 to section 3, indicating the fluctuation of flow magnitude from front region to the tail part of melt pool. Whereas the continuously decreasing tendency of velocity towards melt pool tail is presented in Fig. 5 in sulfur-free situation. In addition, the peak velocity drops when sulfur-effect is modeled. At transverse section 2, it is 1.3 m/s in the 0.03% sulfur while 1.48 m/s in sulfur-free situation. One

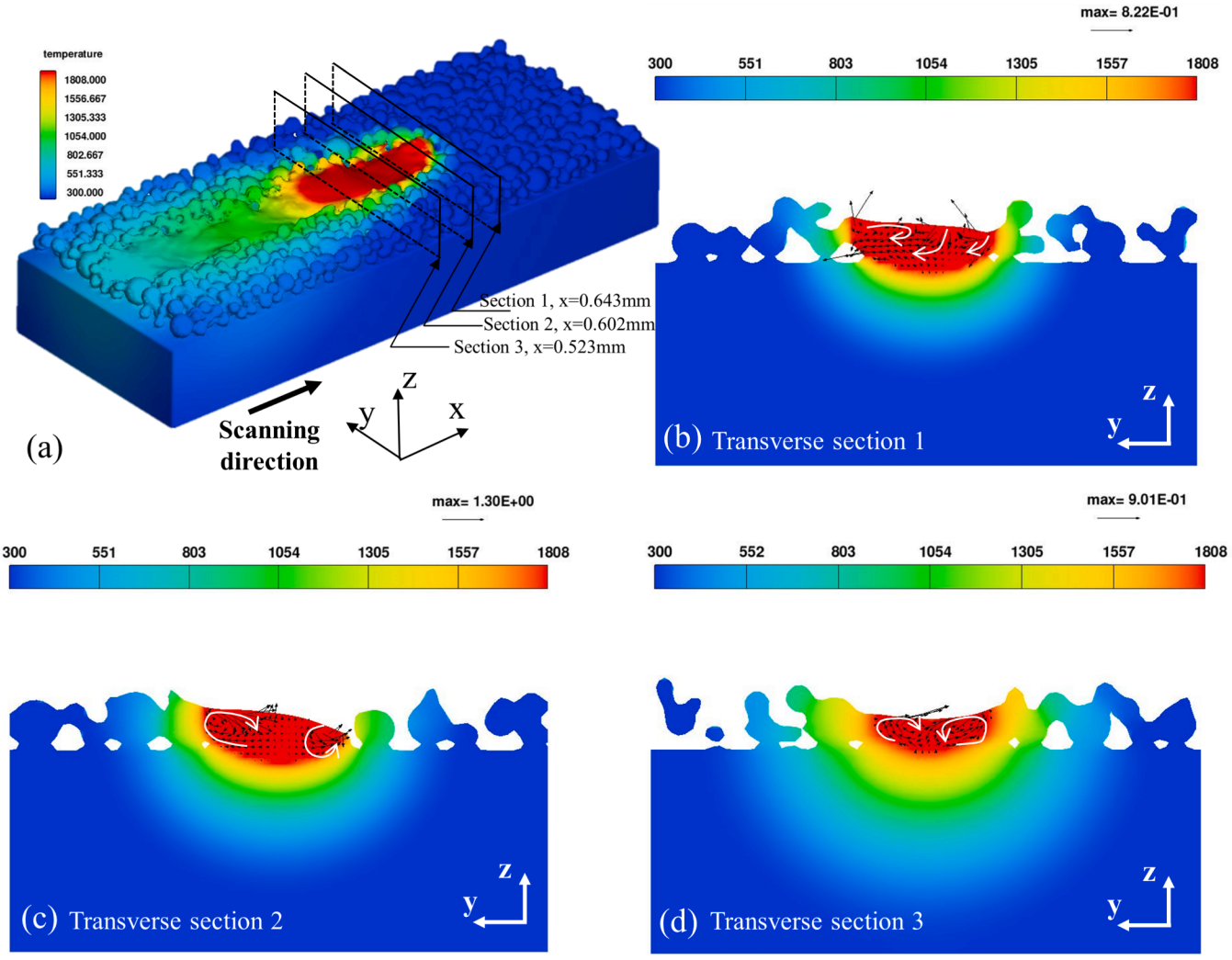

Fig. 12. Temperature distribution and velocity field at transverse view in 0.03% sulfur situation when melt pool is stable. Temperature field in Kelvin is represented by color contour. Flow direction and velocity magnitude (m/s) are depicted by the direction and length of black arrows, respectively. Positions of different transverse sections are labeled in (a) by black rectangle. (a) 3D temperature distribution and velocity field. (b) Temperature distribution and velocity field at transverse section 1. (c) Temperature distribution and velocity field at transverse section 2. (d) Temperature distribution and velocity field at transverse section 3. (For interpretation of the references to color in this figure legend, the reader is referred to the web version of this article.)

underlying reason for the drop of velocity in 0.03% sulfur situation is that the flow dynamics with more vortexes induces more homogenous temperature distribution and reduces the spatial gradient of temperature at gas/liquid surface. As a result, the thermo-capillary force, which is the dominant driving force for flow dynamics, decreases with temperature gradient, leading to smaller driving force and weaker fluid flow.

Melt pool dynamics at different transverse sections in the 0.03% sulfur situation along with the labelled section positions are depicted in Fig. 13. At longitudinal section 1, the decreasing tendency of velocity field towards melt pool tail is still observed but the backward branch flow shown in Fig. 6(b) in the sulfur-free situation changes to a significant frontward flow in Fig. 13(b) in 0.03% sulfur situation. As discussed, the front-to-back flow transports melted materials backwards, increasing the surface roughness of the as-built components. Obviously, the back-to-front flow in 0.03% situation induces a frontward transportation, which is beneficial for the elimination of rough surface. Interestingly, the front-to-back branch flow observed in sulfur-free situation disappears and all the branch flows at longitudinal are towards melt pool head in 0.03% sulfur situation.

As illustrated, the transitions of TCST and flow pattern can be induced in 0.03% sulfur situation, increasing the flow complexities. As shown at longitudinal view in Fig.13, the directions of convection and branch flow are highlighted by white solid arrows, and the defined mixing position of branch flow (MPBF), in which the branch flows with different directions are mixed, is labeled by green dotted rectangle. MPBF makes a difference in the longitudinal view from the sections 1–3 in 0.03% sulfur situation. Compared with the longitudinal flow shown in Fig. 6 in the sulfur-free situation, the number of MPBF has significantly increased due to the sulfur-induced transition of flow pattern. In conclusion, melt pool dynamics is more complex in 0.03% sulfur situation with more branch flow and more MPBF. Thus, it can be concluded that melt pool dynamics will be largely affected by the presence of sulfur element [4], and it provides a potential approach to achieve the processing control by adjusting the fraction of sulfur element contained in powders, enabling the optimization of process-induced structure and the improvement of process-structure related properties.

A comprehensive investigation of melt pool dynamics from 3D view is necessary, thus flow dynamics at z-axis section in 0.03% sulfur situation is analyzed in Fig. 14. At z-axis section 1, the melt pool is filled with liquid materials in the 0.03% sulfur situation without the blank area observed in Fig. 7(b). Therefore, the fluctuation of the melt track along the building direction of as-built components (z direction under Cartesian) has been attenuated by sulfur-effect, which is consistent with the discussion in Fig. 13. Moreover, at the z-axis section 1, two more separate vortices are generated in 0.03% sulfur situation, as well as a significant branch flow towards the head of melt pool. At z-axis section 2 in Fig. 14(c), it is interesting that a regular centrally outward flow is observed. The flow direction is anticlockwise at transverse view (see the schematic inset), thus the centrally outward flow from z-axis view exists near the melt pool bottom, which is observed in both the z-axis sections 2 and 3. Along the direction of melt pool depth, the maximum velocity continues to decrease from the z-axis sections 1–3, indicating that the convection is strong near top surface and weak near the bottom. Despite the transition of flow pattern in 0.03% sulfur situation, this decreasing tendency along depth direction is consistent with that in sulfur-free situation because the fluid flow is driven by thermo-capillary force acting on the melt pool surface in both situations.

3.4. Impact of sulfur content on melt pool dynamics

A parametric study of the contained sulfur concentration will be carried out to explore its impacts on thermo-capillarity and resulting dynamics transition, considering the permitted maximum sulfur content in 316L and its worldwide equivalent alloys. As discussed, the sulfur element contained in 316L is a key factor for melt pool dynamics in L-PBF. However, as shown in Fig. 15, the permitted maximum sulfur content in 316L and its worldwide equivalent alloys varies significantly with different standards. Thus, a parametric study by varying the sulfur concentration is necessary to attempt to physically reveal the impact of sulfur content in L-PBF of 316L powders produced in different countries or areas.

Case ID, as well as the corresponding sulfur content for the parametric study is listed in Table 1. Sul-6 is investigated formerly regarding

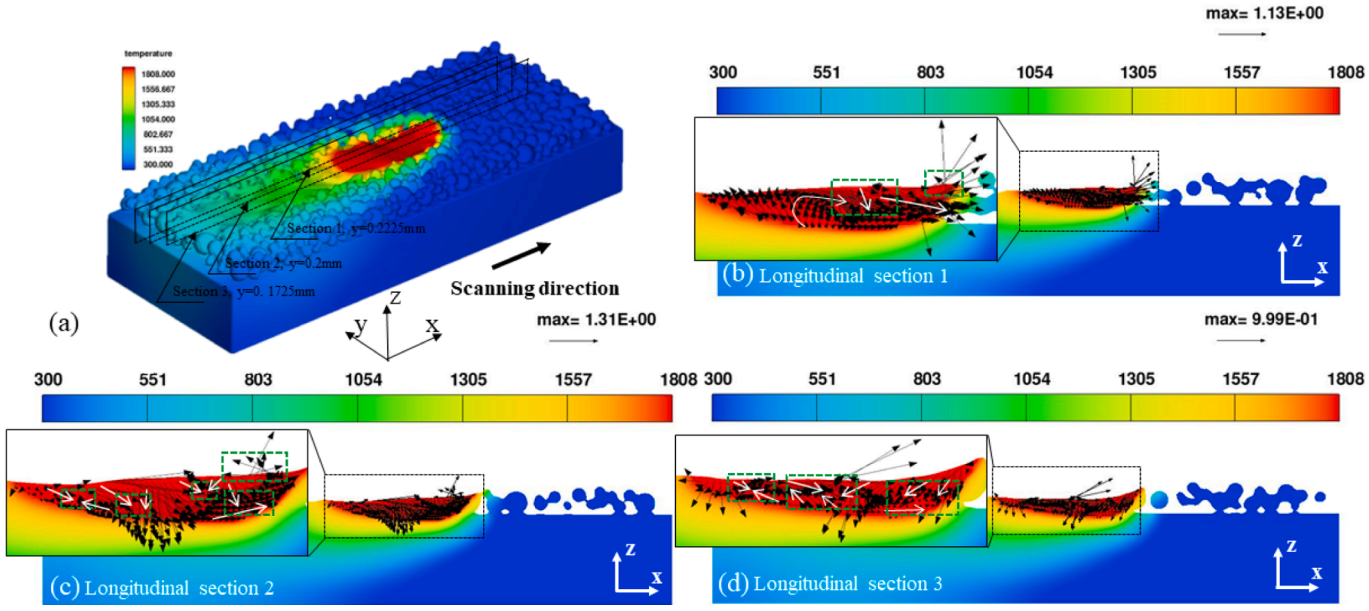

Fig. 13. Temperature distribution and velocity field at longitudinal view in 0.03% sulfur situation when melt pool is stable. Temperature field in Kelvin is represented by color contour. Flow direction and velocity magnitude (m/s) are depicted by the direction and length of black arrows, respectively. Positions of different longitudinal sections are labeled in (a) by black rectangle. (a) 3D temperature distribution and velocity field. (b) Temperature distribution and velocity field at longitudinal section 1. (c) Temperature distribution and velocity field at longitudinal section 2. (d) Temperature distribution and velocity field at longitudinal section 3. (For interpretation of the references to color in this figure legend, the reader is referred to the web version of this article.)

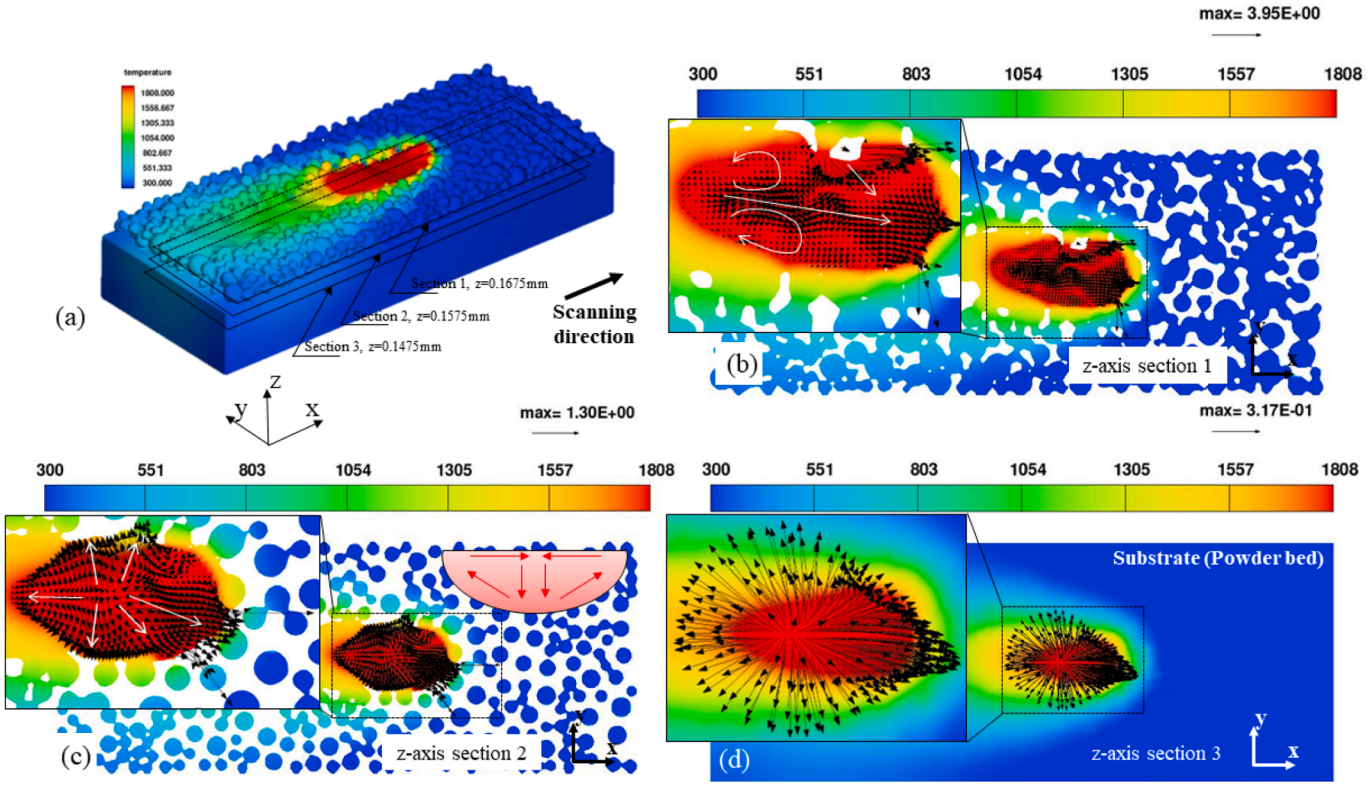

Fig. 14. Temperature distribution and velocity field at z-axis section in 0.03% sulfur situation when melt pool is stable. Temperature field in Kelvin is represented by color contour. Flow direction and velocity magnitude (m/s) are depicted by the direction and length of black arrows, respectively. Positions of different transverse sections are labeled in Fig. 12(a) by black rectangle. (a) 3D temperature distribution and velocity field. (b) Temperature distribution and velocity field at z-axis section 1. (c) Temperature distribution and velocity field at z-axis section 2. (d) Temperature distribution and velocity field at z-axis section 3. (For interpretation of the references to color in this figure legend, the reader is referred to the web version of this article.)

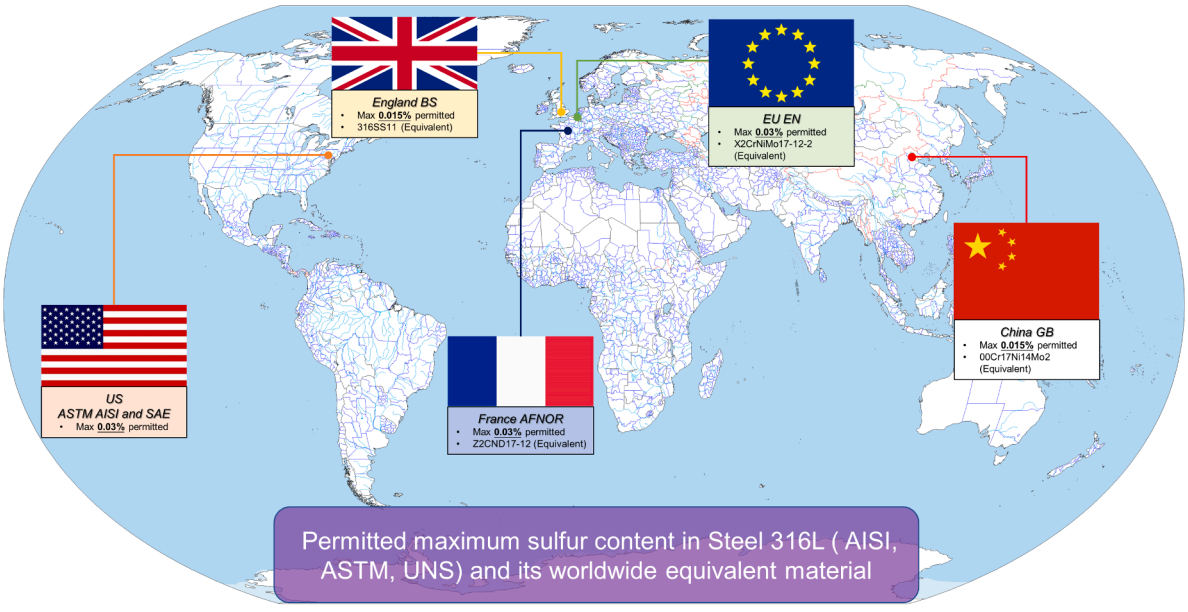

Fig. 15. Permitted maximum sulfur content in 316L and its worldwide equivalent materials, according to different standards. All the insets come from https://cn.bing.com/. (For interpretation of the references to color in this figure legend, the reader is referred to the web version of this article.)

to the US ASTM AISI and SAE, France AFNOR, and EU EN, while Sul-5 is studied in terms of the standards of China GB and England BS. Sul-1 is analyzed with the consideration of extremely low situation. Sul-2, Sul-3, and Sul-4 are performed to probe the transition mechanism. Processing conditions are the same to all six cases for a reliable comparison. Fig. 16 shows the function plots of surface tension and TCST versus local temperature under different sulfur contents. As illustrated in Fig. 16(a), the sign transition of TCST that denotes thermo-capillary transition is absent only in Sul-1 when sulfur content is 0.0001% while it is observed from Sul-2 to Sul-6 when sulfur content is no less than 0.001%. Based on the

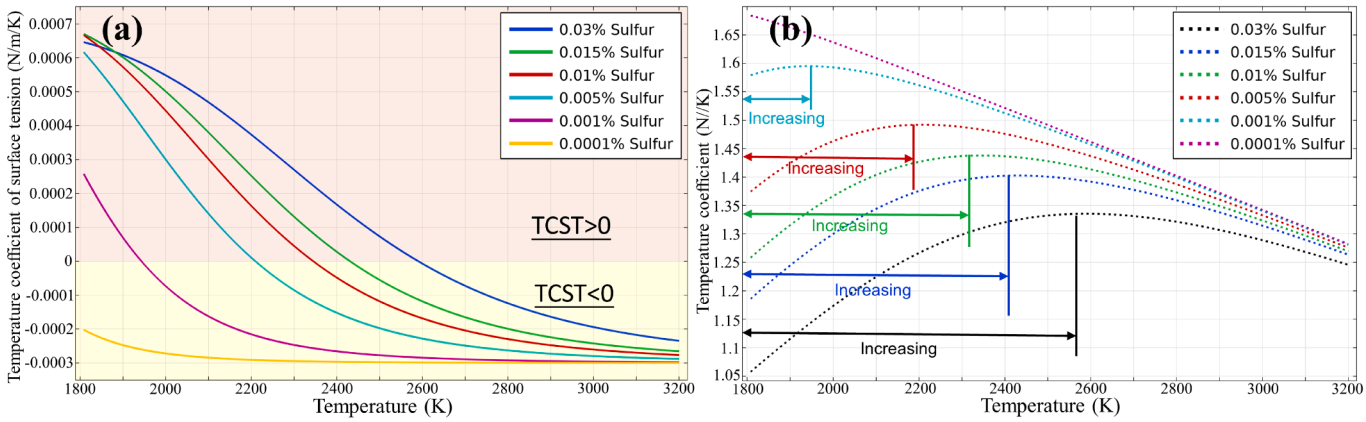

Fig. 16. Plots of temperature coefficient of surface tension (TCST) and surface tension as the function of local temperature in Kelvin and sulfur content in percentage. (a) TCST versus temperature under different sulfur contents. (b) Surface tension versus temperature under different sulfur contents. (For interpretation of the references to color in this figure legend, the reader is referred to the web version of this article.)

mathematical relation of TCST and surface tension described in Figs. 8 and 9, the functional plots of surface tension versus local temperature under different sulfur contents are obtained in Fig. 16(b). Surface tension continuously decreases in Sul-1 due to its negative TCST. In contrast, it increases when TCST is positive then drops when TCST is negative for the other five cases. It indicates that sulfur-effect on melt pool dynamics is not negligible though its concentration is extremely low in additive manufacturing of metallic powders. The occurrence of TCST, TCST transition temperature, as well as the flow pattern at top view as a function of sulfur content are summarized and listed in Table 5. As shown, the transition temperature of TCST continuously increases with the increment of sulfur content. Moreover, the flow pattern is absolutely outward in Sul-1 while it is the combined flow pattern as the coexistence of TCST (−) and TCST (+).

The stable melt pools with the sulfur contents of Sul-1 (0.0001%), Sul-2 (0.001%), and Sul-5 (0.015%) are plotted in Fig. 17. Liquid region label ranges from zero to one in Fig. 17, representing the fraction of liquid phase in modeling results. Thus, the melt pool is colored by red contour at different views, as well as highlighted by white dotted rectangle. As illustrated, process-induced defects in L-PBF including balling, pores/voids, and discontinuity, etc., are not observed in Sul-1, Sul-2, and Sul-5. It indicates that current processing parameters are appropriate to obtain defect-free melt track in L-PBF of 316L powders, despite the content of sulfur element has significantly varied.

Table 5
Occurrence of TCST, TCST transition temperature, and flow patter at the top view with the variation of sulfur content.

Case ID	Occurrence of TCST	Transition temperature (K)	Flow pattern (Top view)
Sul-1 (0.0001%)	TCST (−)	NA	
Sul-2 (0.001%)	TCST (+&−)	1942	
Sul-3 (0.005%)	TCST (+&−)	2208	
Sul-4 (0.01%)	TCST (+&−)	2245	
Sul-5 (0.015%)	TCST (+&−)	2430	
Sul-6 (0.03%)	TCST (+&−)	2590	

Interestingly, melt pool dimensions do not vary monotonically with sulfur content. From Sul-1 to Sul-2, in which the sulfur content has increased 10 times from 0.0001% to 0.001%, the melt pool length has greatly increased, followed by an increase in the melt depth, while the melt width changes little. From Sul-2 to Sul-5, in which the sulfur content has increased 15 times from 0.001% to 0.015%, the melt pool length and width have significantly increased, while the melt depth is almost unchanged. In comparison with the melt pool dimensions in sulfur-free situation, which are highlighted by red dotted rectangle in Fig. 17, the melt pool length of Sul-1 is smaller, while it is greater for Sul-2 and Sul-5. Melt pool width is nearly equal for Sul-1 and Sul-2 but significantly increases for Sul-5 compared with the sulfur-free situation. Melt pool depth changes little from sulfur-free situation to Sul-1 but becomes larger in the case of Sul-2 and Sul-5. The quantitative values of melt pool width under different sulfur levels are listed in Table 6. Briefly, sulfur-effect leads to the increase of melt pool dimensions in L-PBF. What is more, it can be concluded that melt pool dimensions are more sensitive at relatively higher sulfur content in powders.

As discussed, dimensional analysis is a strong and powerful tool to obtain the coupled impacts of processing parameters and physical properties of materials on melt pool dynamics [4]. Dimensional analysis plays a significant role on L-PBF because there are multiple parameters and physical properties that act on the evolution of melt pool dynamics, which have greatly increased the complexity and uncertainty of PSP relations in L-PBF [4,47,48]. Therefore, several key dimensionless numbers for six study cases will be analyzed next.

The significance and expression of Reynolds number (Re), Peclet number (Pe) for heat transfer, Grashof number (Gr), and Marangoni number (Ma) are illustrated in Table 4 and not repeated here. Eckert number (Ec) denotes the relative strength of kinematic energy to internal energy and can be expressed as $Ec = U^2/C_p\Delta T$. Prandtl number (Pr) is defined as the ratio of momentum diffusivity to thermal diffusivity and can be calculated by $Pr = \mu C_p/K$. The values of several key variables involving the peak temperature, the maximum velocity, and the averaged absolute value of TCST, represented by $\bar{s}$, are also listed in Table 6.

As listed in Table 7, Re increases with sulfur content, indicating that the role of inertial force becomes more important and the flow instability is increased, because the turbulent motion cannot be compensated by the viscosity in high-sulfur situation. According to the theoretical analysis and experimental observation of fluid flow, the critical Re for pipe flow is ~2300, however, it is still not clear for the melt pool dynamics in L-PBF due to its extreme manufacturing conditions such as

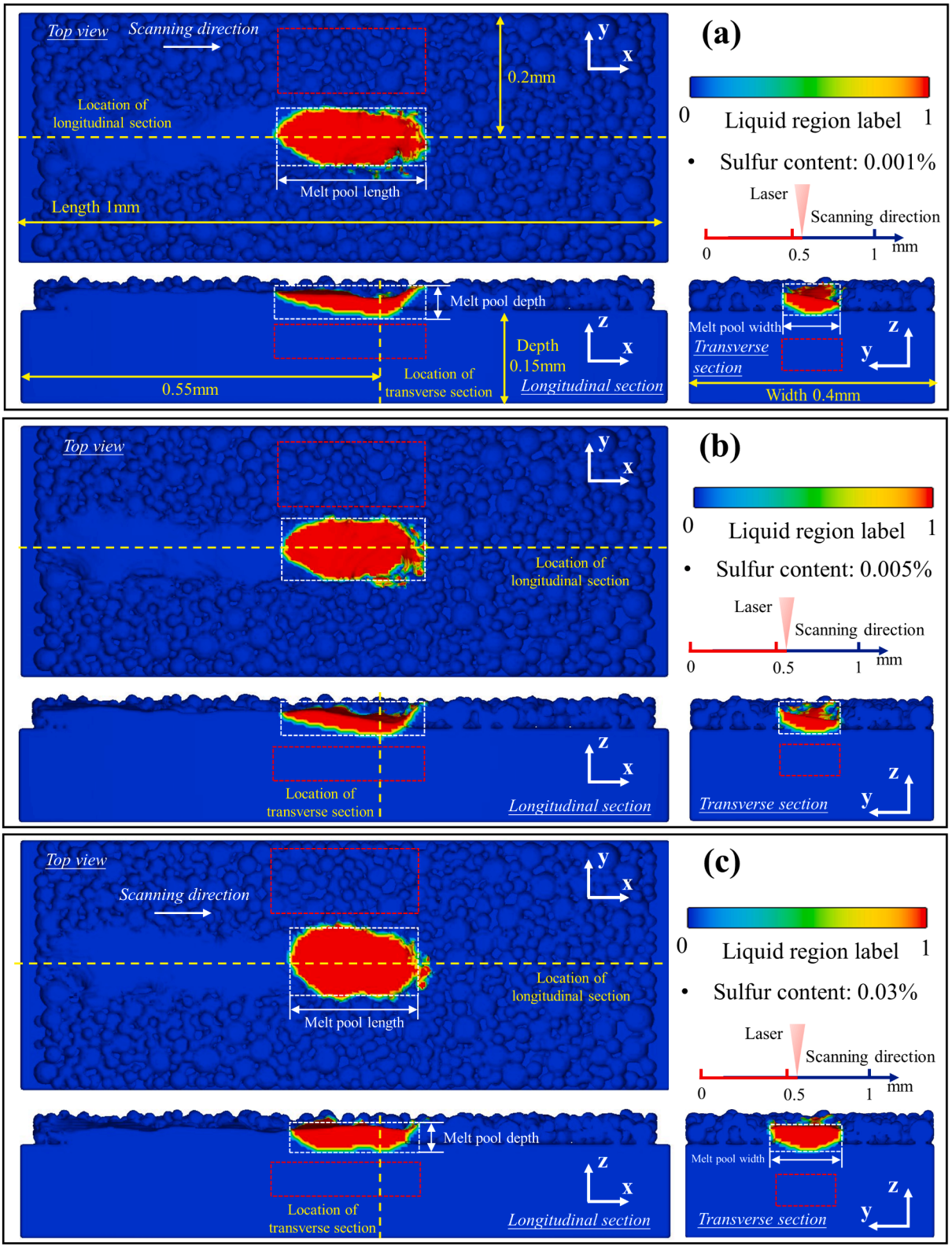

Fig. 17. Melt pool evolution and track morphology at top view, longitudinal section, and transverse section in L-PBF of 316L powders with the consideration of sulfur-effect on melt pool dynamics. Melt pool at different study cases is labeled by white dotted rectangle, and the red dotted rectangle represents the stable melt pool in sulfur-free situation, corresponding to the same printing time of 1100 μs. Positions of longitudinal section and transverse section are illustrated by the yellow dotted line. Color contour represents the fraction of liquid phase. Inset above transverse section describes the location of laser heat source in proposed model corresponding to the real physical time. (a) 0.0001% sulfur content, (b) 0.001% sulfur content, (c) 0.015% sulfur content. (For interpretation of the references to color in this figure legend, the reader is referred to the web version of this article.)

Table 6
Quantitative values of some key variables under different sulfur levels.

Case ID	Sul-1 (0.0001%)	Sul-2 (0.001%)	Sul-3 (0.005%)	Sul-4 (0.01%)	Sul-5 (0.015%)	Sul-6 (0.03%)
Peak temperature (K)	4607	4328	4407	4942	5024	4941
Maximum velocity (K)	5.08	6.45	5.99	6.87	7.98	8.60
Melt pool width (μm)	92	85	84	108	108	120
$\bar{s}$ (N/m/K)	2.885E−4	2.370E−4	2.400E−4	2.500E−4	2.558E−4	2.643E−4

Table 7
Several key dimensionless numbers for melt pool dynamics with the variation of sulfur content.

	Dimensionless numbers						
Case ID	Re	Ec	Pr	Pe	Gr	Ma	$R_{Ma/Gr}$
Sul-1 (0.0001%)	638	1.72E−09	0.140	89.5	0.801	1.69E+04	2.11E+04
Sul-2 (0.001%)	728	3.59E−09	0.140	103	0.523	1.12E+04	2.15E+04
Sul-3 (0.005%)	666	2.87E−09	0.140	93.9	0.515	1.16E+04	2.24E+04
Sul-4 (0.01%)	987	2.38E−09	0.140	137	1.34	1.88E+04	1.40E+04
Sul-5 (0.015%)	1149	3.01E−09	0.140	159	1.38	1.98E+04	1.42E+04
Sul-6 (0.03%)	1368	3.74E−09	0.140	190	1.82	2.19E+04	1.20E+04

high-temperature and high cooling rate. Researchers from welding community have devoted many efforts to explore the impact of turbulence on melt pool dynamics [22,49,50] though the critical Re is still not defined. It has been demonstrated that the neglect of turbulence will result in the over prediction of melt pool width and the weaknesses in the calculation of melt pool depth [50]. Thus, turbulence of melt pool should be given enough attention for high-fidelity simulation in high sulfur situation, which will be further discussed in detail in future work.

Based on the calculated Ec listed in Table 7, Ec is extremely small at the magnitude of 10^{-9} and shows the increasing tendency with the increase of sulfur content. Thus, the internal energy outweights kinematic energy much over for the laser-induced melt pool in L-PBF because the internal energy is only determined by temperature, which is over evaporation temperature from the simulated temperature field shown in Fig. 4 and makes the internal energy much higher. The obtained value of Ec fluctuates among the six cases but its increasing tendency with the increment of sulfur concentration can still be observed, which means that the fluid flow is stronger and kinematic energy becomes higher when sulfur content inside melt pool increases.

Pr is only determined by properties and unchanged for six cases in the current study. The calculated Pr is 0.140 and much smaller than the unit value, representing that the momentum diffusivity plays a more important role in the construction of melt pool morphology. The heat transfer Pe is at the magnitude of 10^2, and shows the growing role of advection as it increases from Sul-1 to Sul-6. It confirms that energy transportation is dominated by convection flow for all the situations and fluid flow inside melt pool is stronger in high-sulfur situation.

Gr, Ma, and the ratio $R_{Ma/Gr}$ are calculated to illustrate the role of driving force on melt pool dynamics. The ratio $R_{Ma/Gr}$ is at the magnitude of 10^4, which means that fluid flow is dominated by surface tension for all the situations. There is an increment of Gr with the increase in sulfur. Gr largely depends on L and ΔT according to its mathematical expression. The sign transition of TCST makes the temperature distribution more uniform [51] attributed to the self-digression phenomenon as it destroys the temperature gradients that contribute to Marangoni effect [52]. As a result, there is a reduction of temperature difference [53]. Although the ΔT is reduced, the melt pool width grows with sulfur content (see Table 6 and Fig. 17). Based on above conclusions, it can be inferred that the increment of Gr is induced by the growth of L. In addition, the calculated Ma continually increases with sulfur content, which depends on ΔT, L, as well as the absolute value of TCST. The variations of TCST versus temperature under different sulfur concentrations are plotted in Fig. 16. The averaged absolute values of TCST for different cases are calculated and listed in Table 6 subject to the following relation, $\bar{s} = \frac{1}{n}\sum_{i=1}^{n} S_i$, in which S_i is the absolute value of TCST corresponding to the i_{th} temperature point and one thousand data points are calculated for each case. The growth of $\bar{s}$ is found with the increasing of sulfur content from Sul-2 to Sul-6, which contributes to the increment of Marangoni number. Whereas the averaged absolute value of TCST for Sul-1 is much higher though its contained sulfur concentration is the lowest. As a result, the obtained Ma for Sul-1 is larger than that for Sul-2 and Sul-3. The increasing tendency of Ma from Sul-2 to Sul-6 indicates that the intensity of Marangoni convection increases with sulfur content when it exceeds a threshold, which may be located between 0.0001% (Sul-1) and 0.001% (Sul-2).

The impact of sulfur content on melt pool dynamics is fundamentally discussed through the modeling and dimensional analysis methods with the consideration of the permitted maximum sulfur content of 316L and its worldwide equivalent materials. More insights into the variations of flow dynamics induced by the difference in sulfur content, such as the spatial and directional characteristics of flow dynamics and transient solidification behavior, etc., will be revealed by the future work focused on the process modeling of L-PBF of 316L powders with different sulfur contents.

4. Conclusion

A powder-scale 3D transient model is proposed to analyze the melt pool dynamics, as well as the sulfur-induced transitions of TCST and flow pattern by coupling the sub-model of surface tension in L-PBF of 316L powders. Fundamental conclusions obtained from modeling and simulation can be summarized as follows.

(1) L-PBF is in conduction mode under current processing parameters. High-temperature area is located at melt pool head and coincides with the position of laser heat source, while the high-velocity parts randomly distribute at different positions of melt pool. Heat transfer is dominated by convective transfer in L-PBF. Fluid flow is dominantly driven by surface tension and the buoyancy force for L-PBF is not strong enough to overcome the restriction from viscous force. From center to the periphery of melt pool in sulfur-free situation, local temperature at gas/liquid surface decreases while the surface tension increases. As a result, a centrally outward Marangoni convection is prompted because fluid flow is directed towards areas with a larger driving force.
(2) Sulfur element contained in 316L powders with the content of 0.03% induces the transition of TCST from positive to negative value with the increasing of local temperature at the gas/liquid surface. As a result, the surface tension first increases and then decreases with the increasing of local temperature from central

area to the melt pool boundary. Melt pool length has dropped but the melt pool width increases in the 0.03% sulfur situation, compared with those in sulfur-free situation. The new flow pattern of combined outward-inward flow is observed because of the sulfur-induced transition of surface tension. In detail, surface tension first increases then decreases from the center to the periphery of the melt pool, which induces the centrally outward flow at central area and the inward flow near melt pool boundary.

(3) At the same transverse section, the maximum velocity decreases in 0.03% sulfur situation because the sulfur-induced complex flow lowers the spatial gradient of temperature and decreases the driving force. Melt pool dynamics in 0.03% sulfur situation are more complex with more vortexes induced at transverse section and more branch flows and mixing positions of branch flow (MPBF) observed at longitudinal section. In detail, the backward branch flow at longitudinal view observed in sulfur-free situation has changed to frontward direction in 0.03% sulfur situation, which is beneficial for the reduction of surface roughness of solidified track. Moreover, blank area is not found at top view in the melt pool in 0.03% sulfur situation. For the melt pool dynamics revealed by z-axis sections, materials flow towards center at top area but change to centrally outwards near the bottom, as a result of the sulfur-induced transition of flow pattern.

(4) Melt pool dimensions are more sensitive to sulfur content in high-concentration situations. Reynolds number increases with the increment of sulfur content and indicates that the flow stability drops in high-sulfur situations. Eckert number shows increasing tendency with the increasing of sulfur content, which means that kinematic energy becomes higher when sulfur content increases. There is an increasing tendency of Marangoni number attributed to the increment of the absolute value of TCST from Sul-2 to Sul-6, which indicates that the intensity of Marangoni convection increases with the increasing sulfur content when it is beyond a threshold.

CRediT authorship contribution statement

Zhiyong Li: Conceptualization, Methodology, Software, Investigation, Funding acquisition. **Xiuli He:** Resources, Data curation, Project administration. **Shaoxia Li:** Validation. **Xinfeng Kan:** Software, Methodology. **Yanjun Yin:** Formal analysis, Validation. **Gang Yu:** Validation, Formal analysis, Resources, Supervision.

Declaration of Competing Interest

The authors declare that they have no known competing financial interests or personal relationships that could have appeared to influence the work reported in this paper.

Data availability

Data will be made available on request.

Acknowledgement

Zhiyong Li acknowledges the supports from National Natural Science Foundation of China (No. 12202448), and Chinese Scholarship Council (CSC).

References

[1] P. Bidare, I. Bitharas, R.M. Ward, M.M. Attallah, A.J. Moore, Fluid and particle dynamics in laser powder bed fusion, Acta Mater. 142 (2018) 107–120.
[2] J. Yin, D. Wang, L. Yang, H. Wei, P. Dong, L. Ke, G. Wang, H. Zhu, X. Zeng, Correlation between forming quality and spatter dynamics in laser powder bed fusion, 31 (2020) 100958.
[3] H. Chen, W.T. Yan, Spattering and denudation in laser powder bed fusion process: Multiphase flow modelling, Acta Mater. 196 (2020) 154–167.
[4] T. Debroy, H.L. Wei, J.S. Zuback, T. Mukherjee, J.W. Elmer, J.O. Milewski, A. M. Beese, A. Wilson-Heid, A. De, W. Zhang, Additive manufacturing of metallic components–process, structure and properties, Prog. Mater Sci. 92 (2018) 112–224.
[5] J.H. Zhu, H. Zhou, C. Wang, L. Zhou, S.Q. Yuan, W.H. Zang, A review of topology optimization for additive manufacturing: Status and challenges, Chin. J. Aeronaut. 34 (1) (2021) 91–110.
[6] D.D. Gu, W. Meiners, K. Wissenbach, R. Poprawe, Laser additive manufacturing of metallic components: materials, processes and mechanisms, Int. Mater. Rev. 57 (3) (2012) 133–164.
[7] Z. Li, G. Yu, X. He, S. Li, C. Tian, B. Dong, Analysis of surface tension driven flow and solidification behavior in laser linear welding of stainless steel, Opt. Laser Technol. 123 (2020).
[8] D.D. Gu, X.Y. Shi, R. Poprawe, D.L. Bourell, R. Setchi, J.H. Zhu, Material-structure-performance integrated laser-metal additive manufacturing, Science 372 (6545) (2021) 1487.
[9] Q. Guo, C. Zhao, L.I. Escano, Z. Young, L. Xiong, K. Fezzaa, W. Everhart, B. Brown, T. Sun, L. Chen, Transient dynamics of powder spattering in laser powder bed fusion additive manufacturing process revealed by in-situ high-speed high-energy x-ray imaging, Acta Mater. 151 (2018) 169–180.
[10] V. Gunenthiram, P. Peyre, M. Schneider, M. Dal, F. Coste, I. Koutiri, R. Fabbro, Experimental analysis of spatter generation and melt-pool behavior during the powder bed laser beam melting process, J. Mater. Process. Technol. 251 (2018) 376–386.
[11] P. Bidare, I. Bitharas, R.M. Ward, M.M. Attallah, A.J. Moore, Laser powder bed fusion in high-pressure atmospheres, Int. J. Adv. Manuf. Technol. 99 (1-4) (2018) 543–555.
[12] M.J. Matthews, G. Guss, S.A. Khairallah, A.M. Rubenchik, P.J. Depond, W.E. King, Denudation of metal powder layers in laser powder bed fusion processes, Acta Mater. 114 (2016) 33–42.
[13] T.G. Spears, S.A. Gold, In-process sensing in selective laser melting (SLM) additive manufacturing, Integr. Mater. Manuf. Innov. 5 (1) (2016) 16–40.
[14] H. Krauss, T. Zeugner, M.F. Zaeh, Layer wise monitoring of the selective laser melting process by thermography, Phys. Procedia 56 (2014) 64–67.
[15] X. Kan, Y. Yin, D. Yang, W. Li, J. Sun, Micro pool characteristics of 316L and the influence of sulfur during SLM, Opt. Laser Technol. 142 (2021).
[16] T. Mukherjee, H.L. Wei, A. De, T. Debroy, Heat and fluid flow in additive manufacturing–Part II: Powder bed fusion of stainless steel, and titanium, nickel and aluminum base alloys, Comput. Mater. Sci 150 (2018) 369–380.
[17] G. Vastola, Q.X. Pei, Y.W. Zhang, Predictive model for porosity in powder-bed fusion additive manufacturing at high beam energy regime, Addit. Manuf. 22 (2018) 817–822.
[18] W.J. Ge, S. Han, S.J. Na, J.Y. Hsi Fuh, Numerical modelling of surface morphology in selective laser melting, Comput. Mater. Sci 186 (2021), 110062.
[19] Z. Li, G. Yu, X. He, S. Li, Z. Li, Fluid flow and solute dilution in laser linear butt joining of 304SS and Ni, Int. J. Heat Mass Transf. 161 (2020).
[20] Z.Y. Li, G. Yu, X.L. He, C.X. Tian, S.X. Li, H.M. Li, Probing thermocapillary convection and multisolute dilution in laser welding of dissimilar miscible metal, Int. J. Therm. Sci. 172 (2022), 107242.
[21] P. Sahoo, T. Debroy, M.J. McNallan, Surface tension of binary metal—surface active solute systems under conditions relevant to welding metallurgy, Metall. Mater. Trans. B 19 (3) (1988) 483–491.
[22] S. Kou, Welding Metallurgy, John Wiley & Sons, New York, 2003.
[23] H. Shen, Y.Q. Pan, J. Zhou, Z.Q. Yao, Forming mechanism of bump shape in pulsed laser melting of stainless steel, J. Heat Transf.-T ASME 139 (6) (2017), 062301.
[24] Y. Hu, X. He, G. Yu, S. Li, C. Zheng, W. Ning, Experimental and numerical study on laser keyhole welding of 42CrMo under air and argon atmosphere, Int. J. Adv. Manuf. Technol. 90 (9-12) (2017) 3555–3565.
[25] Z.T. Gan, G. Yu, X.L. He, S.X. Li, Surface-active element transport and its effect on liquid metal flow in laser assisted additive manufacturing, Int. Commun. Heat Mass Transf. 86 (2017) 206–214.
[26] V. Voller, C. Prakash, A fixed grid numerical modelling methodology for convection–diffusion mushy region phase-change problems, Int. J. Heat Mass Transf. 30 (8) (1987) 1709–1719.
[27] A.D. Brent, V.R. Voller, K.J. Reid, Enthalpy-Porosity technology for modeling convection-diffusion phase-change - application to the melting of a pure metal, Numerical Heat Transfer 13 (3) (1988) 297–318.
[28] The World Material, https://www.theworldmaterial.com/.
[29] A. Masmoudi, R. Bolot, C. Coddet, Investigation of the laser-powder-atmosphere interaction zone during the selective laser melting process, J. Mater. Process. Technol. 225 (2015) 122–132.
[30] M. Courtois, M. Carin, P. Le Masson, S. Gaied, M. Balabane, Guidelines in the experimental validation of a 3D heat and fluid flow model of keyhole laser welding, J. Phys. D Appl. Phys. 49 (15) (2016).
[31] Z.Y. Mu, X. Chen, Z.C. Zheng, A.G. Huang, S.Y. Pang, Laser cooling arc plasma effect in laser-arc hybrid welding of 316L stainless steel, Int. J. Heat Mass Transf. 132 (2019) 861–870.
[32] W.T. Yan, W.J. Ge, Y. Qian, S. Lin, B. Zhou, W.K. Liu, F. Lin, G.J. Wagner, Multi-physics modeling of single/multiple-track defect mechanisms in electron beam selective melting, Acta Mater. 134 (2017) 324–333.
[33] W.H. Kim, S.J. Na, Heat and fluid flow in pulsed current GTA weld pool, Int. J. Heat Mass Transf. 41 (21) (1998) 3213–3227.
[34] M. Carin, E. Favre. Numerical Simulation of Fluid Flow during Arc Welding. COMSOL Multiphysics User's Conference, 2005, Paris.

[35] A. Bahrami, D.T. Valentine, B.T. Helenbrook, D.K. Aidun, Study of mass transport in autogenous GTA welding of dissimilar metals, Int. J. Heat Mass Transf. 85 (2015) 41–53.
[36] N. Chakraborty, The effects of turbulence on molten pool transport during melting and solidification processes in continuous conduction mode laser welding of copper–nickel dissimilar couple, Appl. Therm. Eng. 29 (17-18) (2009) 3618–3631.
[37] X. He, J.W. Elmer, T. DebRoy, Heat transfer and fluid flow in laser microwelding, J. Appl. Phys. 97 (8) (2005), 084909.
[38] M. Bayat, S. Mohanty, J.H. Hattel, A systematic investigation of the effects of process parameters on heat and fluid flow and metallurgical conditions during laser-based powder bed fusion of Ti6Al4V alloy, Int. J. Heat Mass Transf. 139 (2019) 213–220.
[39] Y. Zhao, K. Aoyagi, K. Yamanaka, A. Chiba, Role of operating and environmental conditions in determining molten pool dynamics during electron beam melting and selective laser melting, Addit. Manuf. 36 (2020).
[40] M.J. Xia, D.D. Gu, G.Q. Yu, D.H. Dai, H.Y. Chen, Q.M. Shi, Porosity evolution and its thermodynamic mechanism of randomly packed powder-bed during selective laser melting of Inconel 718 alloy, Int. J. Mach. Tool Manu. 116 (2017) 96–106.
[41] Z.Y. Li, G. Yu, X.L. He, S.X. Li, Z. Shu, Surface tension-driven flow and its correlation with mass transfer during L-DED of Co-based powders, Metals 12 (5) (2022) 842.
[42] T. Mukherjee, J.S. Zuback, W. Zhang, T. Debroy, Residual stresses and distortion in additively manufactured compositionally graded and dissimilar joints, Comput. Mater. Sci. 143 (2018) 325–337.
[43] Y.W. Hu, X.L. He, G. Yu, S.S. Zhao, Capillary convection in pulsed butt welding of miscible dissimilar couple, Proc. Inst. Mech. Eng. C J. Mech. Eng. Sci. 231 (13) (2016) 2429–2440.
[44] C. Zhang, J. Zhou, H. Shen, Role of capillary and thermocapillary forces in laser polishing of metals, J. Manuf. Sci. Eng. 139 (4) (2017) 041019–104101.
[45] W.T. Yan, Multi-scale Multi-physics Modeling of Electron Beam Selective Melting Process, Thesis for PhD, Tsinghua University, 2017.
[46] E. Li, Z. Zhou, L. Wang, R. Zou, A. Yu, Numerical studies of melt pool and gas bubble dynamics in laser powder bed fusion process, Addit. Manuf. 56 (2022).
[47] Z. Wang, M. Liu, Dimensionless analysis on selective laser melting to predict porosity and track morphology, J. Mater. Process. Technol. 273 (2019).
[48] T. Mukherjee, V. Manvatkar, A. De, T. DebRoy, Dimensionless numbers in additive manufacturing, J. Appl. Phys. 121 (6) (2017), 064904.
[49] N. Chakraborty, The effects of turbulence on molten pool transport during melting and solidification processes in continuous conduction mode laser welding of copper nickel dissimilar couple, Appl. Therm. Eng. 29 (17-18) (2009) 3618–3631.
[50] Z.Y. Li, G. Yu, X.L. He, S.X. Li, H.M. Li, Q.Y. Li, Study of thermal behavior and solidification characteristics during laser welding of dissimilar metals, Results Phys. 12 (2019) 1062–1072.
[51] L. Jiao, Z.B. Wang, R. Chen, X. Zhu, Q. Liao, D.D. Ye, B. Zhang, W. Li, D.L. Li, Simulation on the Marangoni flow and heat transfer in a laser-heated suspended droplet, Chem. Eng. Sci. 209 (14) (2019), 115202.
[52] J. Betz, J. Straub, Numerical and experimental study of the heat transfer and fluid flow by thermocapillary convection around gas bubbles, Heat Mass Transf. 37 (2-3) (2001) 215–227.
[53] M. Bayat, V.K. Nadimpalli, D.B. Pedersen, J.H. Hattel, A fundamental investigation of thermo-capillarity in laser powder bed fusion of metals and alloys, 166 (2021) 120766.